Temperature Dependence of the HartRAO Pointing Model

A thesis submitted in fulfilment of the
requirements for the degree of

MASTER OF SCIENCE

of

RHODES UNIVERSITY

by

CHARLES JUDD COPLEY

JANUARY 2008

Abstract

This thesis investigates control aspects of the Hartebeeshoek Radio Astronomy Observatory (HartRAO) antenna. The installation of a new 22 GHz receiver has required the pointing accuracy to be improved to less than 4 mdeg.

The effect of thermal conditions on the the HartRAO antenna pointing offset is investigated using a variety of modelling techniques including simple geometric modelling, neural networks and Principal Component Analysis (PCA).

Convincing results were obtained for the Declination pointing offset, where applying certain model predictions to observations resulted in an improvement in Declination pointing offset from 5.5 mdeg to 3.2 mdeg (≈50%). The Right Ascension pointing model was considerably less convincing with an improvement of approximately from 5.5 mdeg to 4.5 mdeg (≈20%) in the Right Ascension pointing offset.

The Declination pointing offset can be modelled sufficiently well to reduce the pointing offset to less than 4 mdeg, however further investigation of the underlying causes is required for the Right Ascension pointing offset.

Acknowledgements

I would first and foremost like to thank my supervisors for their help over the past two years. Prof. Justin Jonas has always taken time out of a very busy schedule to give both advice and assistance. Dr. Jonathan Quick has given valuable insights into the thermal pointing problem during my trips to HartRAO and the late Dr. Paul Nathanson has been a model to aspire to throughout my Rhodes University career.

The staff at HartRAO have always been willing to provide assistance. Mr. Pieter Stronkhorst, Dr. Mike Gaylard, Mr. Keith Jones, Dr. Adrian Tiplady and Mr. Paul Manners all helped a great deal while I was stationed at HartRAO. Paul did an unenviable task of tracing a particular wire through a maze of others for which I am most grateful.

The technical support from Mr. Antony Sullivan at Rhodes has been superb. Without it there would have been many additional hours of pointless head banging. Andrew Youthed provided good experiential advice with board design, and the rest of the Rhodes University Masters students have always been there with a good sense of humour.

I am most grateful for the financial support from DAAD, HartRAO and Rhodes University in the form of the Rhodes University Postgraduate Scholarship. These have been exceptionally generous and have made the time spent researching a great deal more comfortable. I would also like to thank John Gillam and the team at Postgraduate Funding for being both efficient and friendly.

I also acknowledge the data analysis facilities provided by the Starlink Project which is run by CCLRC on behalf of PPARC.

Last but not least I would like to thank my family for their unconditional support over the years. This has been of great comfort to me.

Contents

List of Figures

List of Tables

Chapter 1

Introduction

1.1 Overview of Thesis

1.1.1 Astronomy as a Priority in South Africa

Astronomy has been listed as a priority for South African science as a result of the Astronomy Geographic Advantage Programme. Recent years have seen South Africa emerging as a leading contender to host a number of prestigious astronomical instruments. In the optical domain, the Southern African Large Telescope (SALT) has been built at the South African Astronomical Observatory (SAAO) site in Sutherland, Northern Cape. The world has not lost sight of South Africa's numerous advantages with regards radio telescopes either and South Africa has been shortlisted, alongside Australia, to host the world's most ambitious radio telescope, the Square Kilometre Array (SKA).

As a precursor to the announcement of the winning SKA bid, South Africa is currently building a smaller array called *Meer*KAT, an SKA science and technology demonstrator. The aim behind the project is to build a world-class scientific instrument, develop local expertise and to demonstrate South Africa's ability and commitment to hosting the SKA.

1.1.2 Relevance of Thesis to *Meer*KAT

One of the aspects that needs to be investigated and developed for *Meer*KAT is a model of thermally induced pointing offsets. It is well known that pointing offsets dramatically reduce the dynamic range of mosaic images produced by array telescopes as well as effecting the sensitivity (and thus consistency) of single dish observations (Ukita, 1999).

This thesis investigates thermally induced pointing offsets seen on the HartRAO antenna. A recent receiver upgrade means that modelling these effects is now necessary at HARTRAO and gaining an understanding of the thermal effects on antenna pointing with regards *Meer*KAT will be useful.

1.2 Background

In February 2007, Hartebeeshoek Radio Astronomy Observatory (HartRAO) commissioned and installed a new 1.3 cm (22 GHz) receiver. Previously, the highest observing frequency had been 12 GHz (2.5 cm). Since the approximate beamwidth is given by $\theta_{HPBW} = \frac{1.2\lambda}{D}$ (where λ is the observation wavelength and D is the telescope diameter), this upgrade will result in nearly halving the smallest beamwidth from 80 mdeg to approximately 40 mdeg.

1.2.1 Required Pointing Accuracy

In general, 'blind' radio telescope pointing needs to be accurate to 1/10th of the beamwidth, with array telescopes making interferometric measurements (such as *Meer*KAT) requiring even greater accuracies. This requirement maintains pointing to well inside a window of 1/5th of the beamwidth. Anything larger than this results in a greater than 10% loss of sensitivity of the receiver (Ukita, 1999), causing inconsistent observations which should be avoided. The consequence of this is that the HartRAO telescope pointing accuracy will need to be improved to approximately 4 mdeg (or 1/10 of the beamwidth) as a requirement for consistent observations using the new receiver.

1.2.2 Modelling the Pointing Offset

A number of potential causes of pointing offsets need to be considered when pointing a telescope. These effects include:

- Gravitational deformation of the antenna structure and surface
- Axis Encoder Offsets
- Axis misalignments
- Atmospheric Refraction
- Wind Loading on the antenna structure and surface
- Thermal deformations of the structure and surface

The telescope at HartRAO uses the VLBI pointing model (further detail available in Appendix B) to remove the non-temporal effects such as gravitational deformations, axis misalignments and encoder offsets together with a standard refraction model to account for atmospheric refraction effects, however neither of these models include corrections for temporal effects such as thermal and wind loading.

Increasing the required pointing accuracy means that thermally induced pointing offsets can no longer be considered insignificant and need to be modelled and incorporated into the current pointing correction models. This thesis deals with an examination of the temperatures of the Declination and Hour Angle axis support struts, and the role that these temperatures may play in causing pointing offsets.

The HartRAO Antenna is equatorially mounted and it should be noted that Hour Angle and Right Ascension are a left-handed and right-handed system related to each other through the local sidereal time. Hour Angle will be used when referring to the local coordinate system of the HARTRAO antenna e.g Hour Angle supports, while Right Ascension will be used when referring to observations e.g Right Ascension pointing offset.

The investigation includes using simple physical models, linear fitting, adaptation of the VLBI pointing model, and neural networks to create a model for the pointing offsets using thermal inputs.

1.3 The Thermal Environment of the HartRAO Antenna

An examination of the thermal environment of the HartRAO antenna is critical to begin understanding the thermally induced pointing offsets experienced at HARTRAO. Throughout this thesis, abbreviations will be used to indicate the position of thermistors recording temperature data. These abbreviations are included in Table 1.1. Figures 1.1 (a) → (c) give an idea of the positions of the supports, the orientation of the supports and approximate positions of the temperature sensors.

Table 1.1: Abbreviations used to indicate thermistor positions.

Label	Description
AT1	Top North West Declination Support Temperature
AT2	Top South West Declination Support Temperature
AT3	Bottom North West Declination Support Temperature
AT4	Bottom South West Declination Support Temperature
AT5	Top North East Declination Support Temperature
AT6	Top South East Declination Support Temperature
AT7	Bottom North East Declination Support Temperature
AT8	Bottom South East Declination Support Temperature
AT9	East Hour Angle Support Temperature
AT10	West Hour Angle Support Temperature

1.3.1 Telescope Structure and Solar Illumination

Figures 1.1a, 1.1b and 1.1c are photographs taken of the HartRAO structure in July 2006, from orthogonal viewpoints at approximately the same height in an effort to obtain the dimensions

of various beams. A simple structural diagram is included in Figure 1.1d. It is important to note the solar illumination on the Declination support beams. Since HARTRAO is in the Southern Hemisphere the Sun always transits across the Northern part of the sky being highest above the horizon in the Summer, and closest to the horizon in the Winter. We see from Figure 1.1a that the Sun illuminates the lower half of the North facing Declination support in July (Winter). Examination of Figure 1.1b shows that the Sun does not illuminate the South Declination support at all at this time. It is clear from this that the North facing beam will generally be warmer than the South facing beam during the day when solar illumination is greatest. The Hour Angle supports do not show similar differences in solar illumination.

1.3.2 Support Temperatures

Temperature data, shown in Figure 1.2 and Figure 1.3, suggests that while the North facing Declination supports are warmer during the day (as expected due to the Solar illumination), the South facing Declination supports may actually be warmer than the North facing side, particularly in the early evening. This may be due to the North facing side undergoing faster radiative cooling after sunset, since it isn't shielded by the antenna support buildings.

Figure 1.2 shows that the temperature differential between the North facing Declination supports and the South facing Declination supports varies both diurnally and, to a lesser extent, with season. Figure 1.3 shows the Hour Angle supports temperatures which do not show this same seasonal variation.

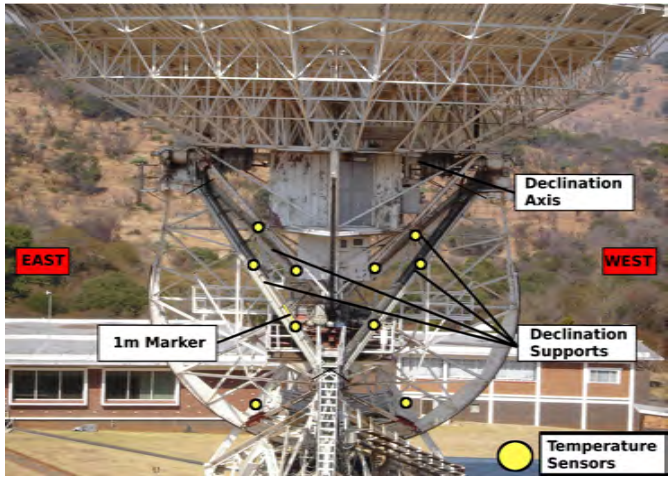

(a) View of Dish from the North. The V-shaped supports are the North facing Declination supports.It is important to note that these are illuminated by the sun. The 1m marker was used to estimate support lengths and was included in all photographs. It is difficult to see in the other examples.

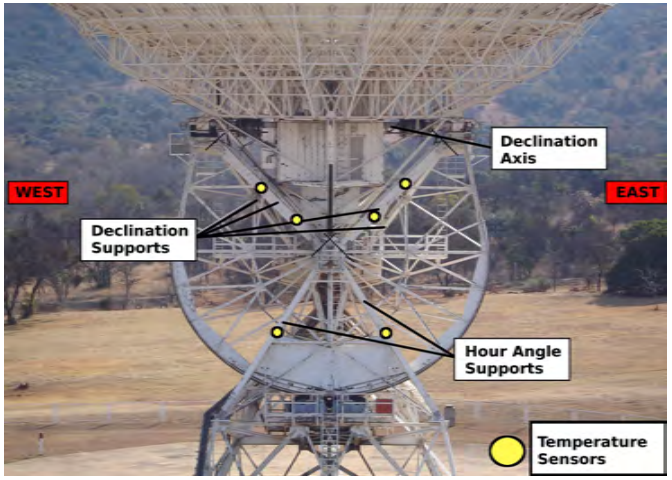

(b) View of Dish from the South. The V-shaped supports are the South facing Declination supports. When compared to Figure 1.1a we see that these supports are not illuminated by the sun.

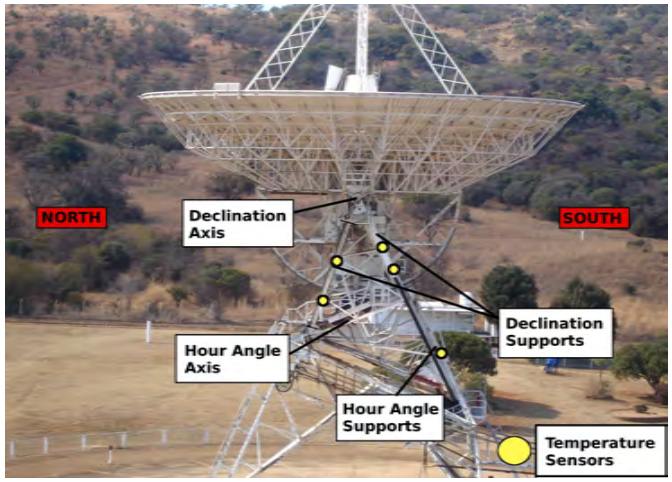

(c) View of Dish from the West

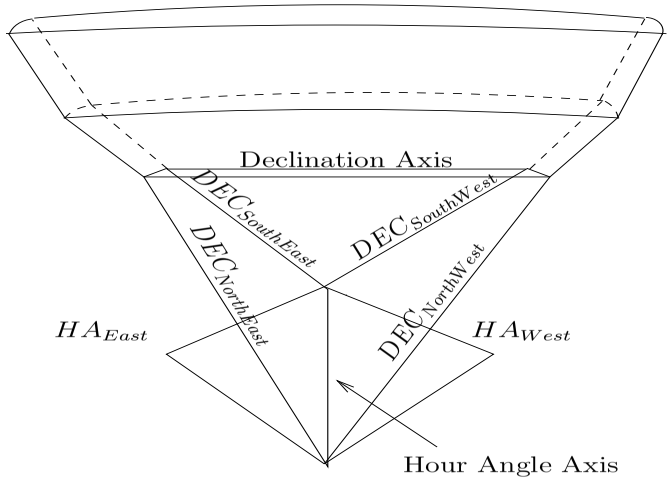

(d) Simplified structure

Figure 1.1: Orthogonal photographs of the HARTRAO dish taken in July 2006. These show the pattern of the solar illumination experienced by the North facing Declination support beams in Figure 1.1a. They indicate the orientation of the different supports in relation to each other and show the positions of temperature sensors.

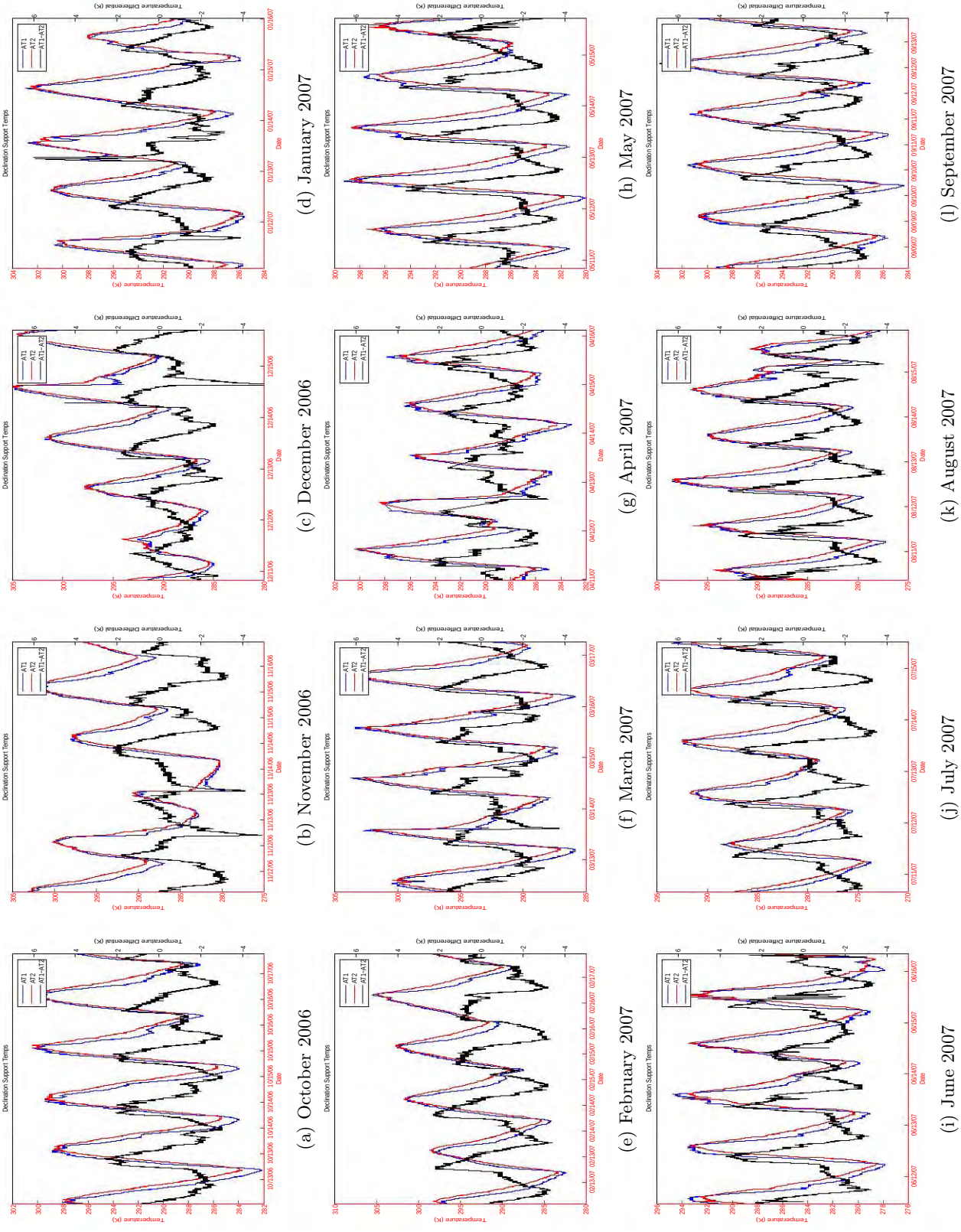

(a) October 2006 (b) November 2006 (c) December 2006 (d) January 2007

(e) February 2007 (f) March 2007 (g) April 2007 (h) May 2007

(i) June 2007 (j) July 2007 (k) August 2007 (l) September 2007

Figure 1.2: Temperature readings (5 days in each month) from the Declination Support mounted thermocouples obtained throughout a complete annual cycle. These figures show the variation in the thermal loading of the supports during the different seasons. AT1 is the temperature at the top of the North West Declination support and AT2 is the corresponding temperature at the top of the South West Declination support.

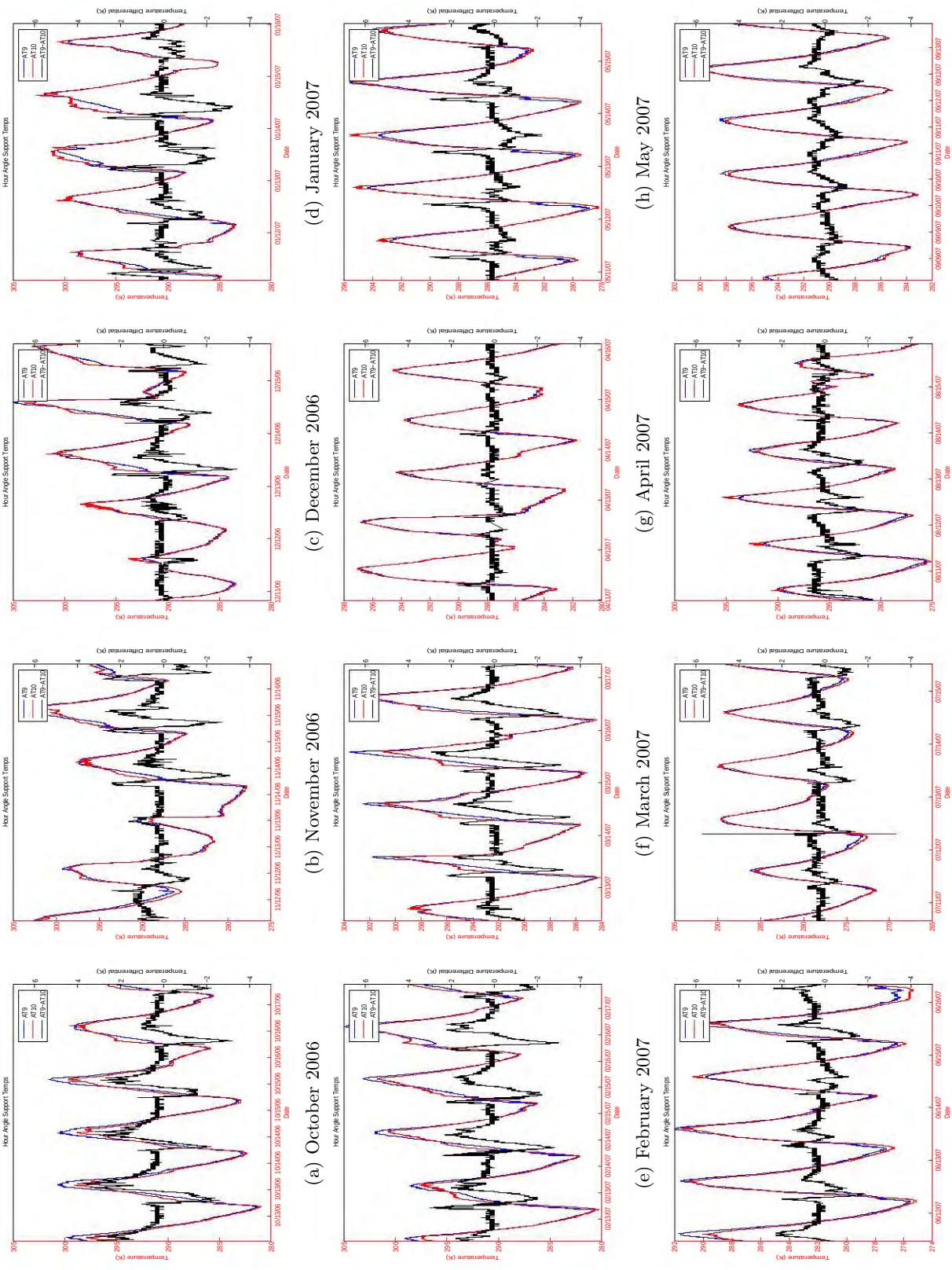

(a) October 2006 (b) November 2006 (c) December 2006 (d) January 2007

(e) February 2007 (f) March 2007 (g) April 2007 (h) May 2007

(i) June 2007 (j) July 2007 (k) August 2007 (l) September 2007

Figure 1.3: Temperature readings from the Hour Angle Support mounted thermocouples obtained throughout the year. AT9 is the East Hour Angle support temperature and AT10 is the West Hour Angle support temperature.

1.4 Previous Models

Previous measurement of the Declination and Hour Angle pointing offsets were done by Dr. George Nicolson prior to this project, and resulted in the development of the existing heuristic thermal model. Unfortunately there is no formal report, however some always illuminating private communication with Dr Nicolson is a very good substitute. The model is a predictive thermal correction that is dependent on day of year and time of day and is shown in Figure 1.4. The model was derived heuristically by examining pointing offsets throughout the year, however it did not use temperature measurements of the structure. These pointing offset measurements were made before extensive modifications were undertaken on the dish surface and counterbalance, which resulted in a changed mass distribution. Depending on the cause of the thermal pointing offsets they may have been effected by the changed mass distribution.

The predictive model in Figure 1.4 shows that the thermal Declination pointing offset was more pronounced in Winter than in Summer. It shows that the greatest Declination offsets were likely to be found during the day time between 07h00 and 15h00. This is similar to the pattern observed with the maximum temperature differential between North and South Declination supports (see Figure 1.2), both diurnally and seasonally.

This similarity provides a basis to investigating temperature differentials as a starting model of the thermal pointing offset experienced by the HartRAO antenna.

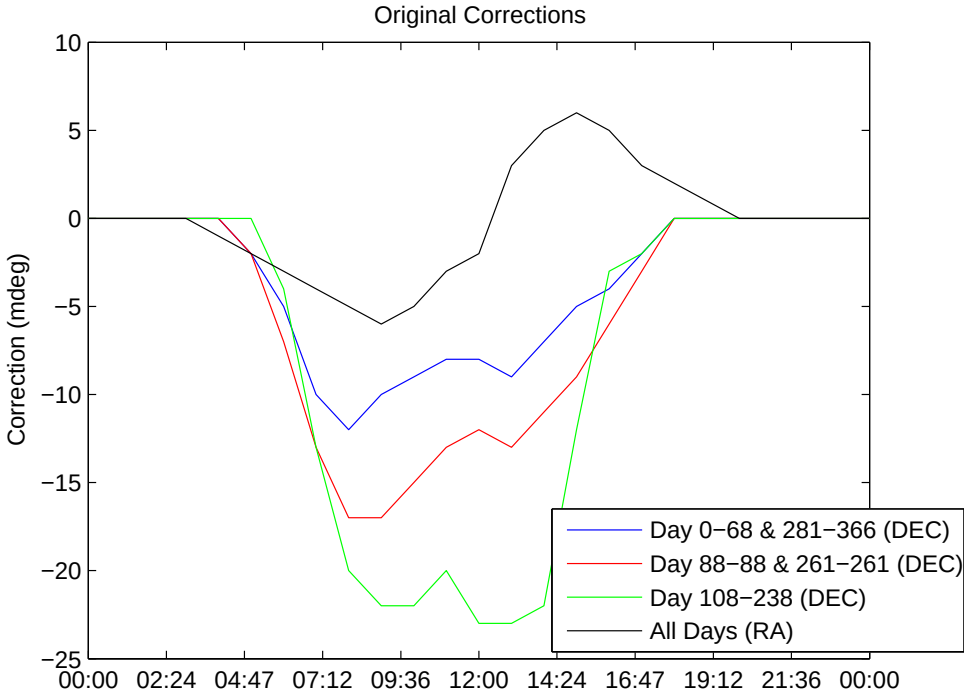

Figure 1.4: The original pointing error correction model derived by Dr. George Nicolson.

1.5 Overview

This thesis begins with a presentation of case studies in Chapter 2. These are all applicable to modelling the thermal pointing offset of the HartRAO telescope. The case studies explore the different modelling methods used in the literature, and explain the relevance of these modelling techniques to the HARTRAO investigation. The case studies include previous pointing offset investigations into the Green Bank Telescope in West Virginia, the MERLIN Telescope in Cambridge, the Leighton 10-m antennas at Owens Valley Radio Observatory in California and the Nobeyama Telescope in Japan. These investigations include Finite Element Analysis models (FEA) (see Section 3.8) and simple geometric modelling as well as a favourable comparison between the two models in the case of the MERLIN and Leighton 10-m antenna investigation. This comparison provides part of the justification for not choosing to use FEA in this investigation.

Chapter 3 presents a theoretical overview of the different modelling techniques used in this study, as well as the general theory behind Finite Element Analysis (FEA). FEA would have been expensive and costly to undertake and may not have given significantly better results (as mentioned earlier with reference to the Leighton 10-m antennas). As such, it was not investigated as a possible methodology, however, it is the most commonly used method

in similar previous studies and therefore deserves mentioning. The existing parameter based VLBI pointing model of HartRAO (which does not account for thermal pointing offsets) is described, a simple geometric model for thermally induced pointing offsets based on thermal expansion of support structures is explained and useful statistical methods such as correlation coefficient matrices and Principal Component Analysis are introduced. The chapter concludes with a discussion of three modelling techniques. These include a least-squares fitting technique, neural network models and FEA.

The data capture and reduction techniques are explained in Chapter 4. It begins by giving an overview of the instrumentation used as well as an outline of the observation strategy. The derivation of pointing offset measurements from radio telescope observations of point sources is explained, and the data reduction strategy is outlined in terms of flow diagrams of the code. Special mention is made of techniques used in flagging and removing poor observations from the data set. The unprocessed pointing observations show an inherent offset which is removed by refitting the VLBI parameters of the HartRAO pointing model and retro-actively applying the new parameters to the pointing observations. This process ensures that the data is not contaminated by any pointing effects modelled in the VLBI pointing model.

Chapter 5, the penultimate chapter of this part of the thesis, describes the results of the modelling techniques outlined earlier in the thesis. The effectiveness of different models are examined in terms of both Right Ascension and Declination pointing offsets. The results show an agreement between Dr. Nicolson's previous pointing observations and the pointing observations obtained during this study. A binning technique clearly shows the relationship between the Declination support temperature differential and the Declination pointing offset and also shows the lack of relationship between the Hour Angle support temperature differential and the Right Ascension pointing offset. A second plot of the two support temperature differentials against the relevent pointing offsets supports the binning technique observation. Principal Component Analysis suggests that the Declination pointing offset is strongly correlated with the second Principal Component, which in turn is strongly correlated with the Declination temperature differential. These results suggest the possibility of modelling the Declination pointing offset using the existing temperature data, while also suggesting that it may not be possible to achieve the same result for the Right Ascension pointing offset. The results of the different modelling techniques described previously are then shown. The different techniques show similar results, reducing the Declination pointing offset by 50% with far less succesful results for the Right Ascension pointing offsets.

Conclusions are then drawn in Chapter 6, and ideas for future research are presented. I touch on the relevance of these results for *Meer*KAT.

Chapter 2

Case Studies

Detailed discussion of the effect of telescope pointing error compensation for thermal structural distortion is not commonly found in the mainstream scientific literature. It is rather found in technical reports (Condon and Constantikes, 2003; Nothnagel et al., 1997) and telescope viability studies (Von Hoemer, 1975). These technical memoranda are fairly brief overviews, aimed primarily at minimising the thermal effect on pointing from the outset by means of material choice, enclosing antennas and structural design. There are a few examples of actual implementation of a correction post-construction (Condon, 2003a; Condon and Constantikes, 2003; Condon et al., 1993; Condon, 2003b). The following sections represent relevent case studies for a selection of telescopes. The unexpected similarity between between Finite Element Analysis[1] (FEA) and simpler models is emphasised.

2.1 Green Bank Telescope

A large number of technical reports from the 100 m Green Bank Telescope (GBT) are available (Condon, 2003a; Condon and Constantikes, 2003; Condon et al., 1993, 1989; Condon, 2003b). These explore attempts made at the GBT to allow observations to be made at up to 117 GHz. Condon (2003a) mentions that if the telescope is much larger than the observing wavelength (i.e $D > 10^4\lambda$ resulting in a small beam), *time-dependent mechanical distortions* are likely to degrade its performance. The reports note that astronomers may have to observe calibration sources periodically in order to maintain the required pointing and tracking tolerances (dictated by the scientific requirements) for aperture efficiency and gain accuracy and consistency (Condon et al., 1993). It is noted that the high sensitivity of the GBT means that a suitable calibrator is typically never more than 0.03 radians from any suitably strong radio source of interest. Since HartRAO is a comparably small antenna, with low sensitivity at 22 GHz, there are few nearby calibrators. Periodic calibration is thus not an option and suitably accurate dead reckoning is required.

[1] See Section 3.8 for a detailed discussion of this technique

2.2 MERLIN Radio Telescope in Cambridge

Bayley et al. (1994) studied the 25 m MERLIN Radio Telescope based in Cambridge. The telescope design is different to HartRAO, being an ALT-AZ mounting, however a number of principles are transferable. Of primary importance are the structural supports of the telescope as shown in Figure 2.1. The elevation configuration is structurally similar to the Declination axis of the HARTRAO antenna shown in Figure 1.1d.

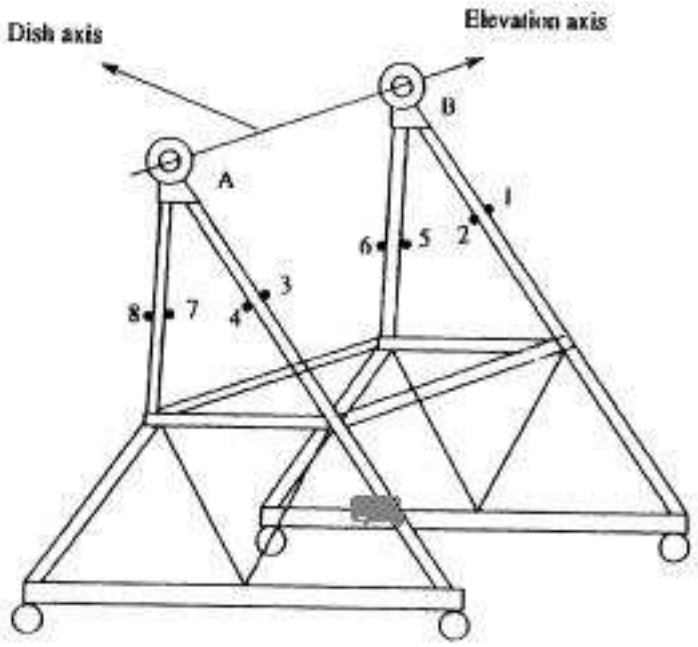

Figure 2.1: The support structure of the MERLIN telescope based at Cambridge together with the positions of the thermistors (Bayley et al., 1994).

The magnitude of the pointing offset observed for the Altitude and Azimuth axes differs, an effect that is observed on the HartRAO antenna Declination and Right Ascension pointing offsets. This paper was able to investigate the use of FEA modelling of the thermal effects on structural distortion, due to the availability of mechanical and structural data (the investigation was carried out immediately after the telescope's commissioning). The result of using FEA predictions in the pointing model, was an improvement of the pointing deviation to approximately 2 mdeg RMS. A simpler model based only on temperature differentials agreed with the FEA predictions to within 0.5 mdeg. A similar agreement between FEA and a simpler model is found on the OVRO Telescope discussed in Section 2.3. This suggests that FEA on simple frame structures such as this may not be necessary. This is a promising result for this study of the HARTRAO antenna, as FEA was not investigated as a methodology due to cost and implementation difficulties.

2.3 Thermal Effects on the Leighton 10 m antennas at Owens Valley Radio Observatory

A detailed study of the backing structure (using FEA) of the Owens Valley Radio Observatory (OVRO) 10 m antennas (Lamb and Woody, 2002) brought attention to the fact that temperatures of the backing structure can effect the focus of the telescope, contributing to other related problems. The investigation is primarily aimed as a pathfinder towards potential problems and solutions for sub-millimetre array telescopes and the emphasis is on using the Leighton 10 m antennas as potential models for these future antenna arrays.

The paper discusses temperature gradients in materials stating that they are a function of the material and the optical and infrared emissivities of the surfaces. This is not relevent to the HartRAO thermal problem, however these are important aspects to be taken into consideration during the construction of *Meer*KAT. Reference is made to dependence on solar illumination, wind and ambient temperature variations which is what this study will focus on.

The problem of an accurate temperature model for the entire structure means that detailed temperature measurements are required. OVRO used 76 thermistors (YSI 44007) mounted on aluminium blocks using thermally conductive epoxy, to obtain temperature readings for modelling the structural deformation. The temperature measurements from the thermistors had an uncertainty of 0.07 °C with a maximum uncertainty of 0.2 °C. The acquisition of temperature data is done in sets of 1000 samples which are averaged to reduce noise and results in measurements that are better than 1 bit on the 12-bit Analogue to Digital converter. The data is recorded every 2 minutes.

The structure was approximately isothermal at night, but during the day significant gradients developed with a maximum thermistor temperature difference of 12 °C observed. Temperature change may occur as quickly as 1.5 C.min^{-1}. The conditions at HartRAO are similar with maximum temperature differences of approximately 10 K and maximum temperature changes of 0.5 C.min^{-1} as shown in Figure 1.2. It was noted that the lowest temperatures on the structure are generally close to ambient air temperature, however they are occasionally lower. This was explained as being partly due to radiative cooling to the sky, and partly due to the 200 m distance to the air temperature sensor from the telescope.

The paper mentions that other telescopes have shown strong astigmatism under solar heating but that this does not appear to be a problem at OVRO. This was not investigated at HartRAO in this study.

A beam-element model (i.e no rotational degrees of freedom at the structural nodes) was

Figure 2.2: Picture of the OVRO 10m Leighton Array

constructed using *Algor* (a FEA program) and is illustrated in Figure 2.3a. The results of the FEA are shown in Figure 2.4. This shows good correlation between the simple linear model (using mean temperature gradients) and the FEA model, although the conclusion is that since the complete FEA solution takes only a few seconds, it is preferable to use the full FEA model. Bayley et al. (1994) notes a similar agreement between FEA and a much simpler model for the MERLIN telescope as described in Section 2.2. This is a promising result for HartRAO since the models explored here do not include FEA. However, since the OVRO results are based on modelling the backing structure as per Figure 2.3a, it does suggest that the pointing offset at HARTRAO may be caused by thermal gradients in areas other than the Declination and Hour Angle support struts.

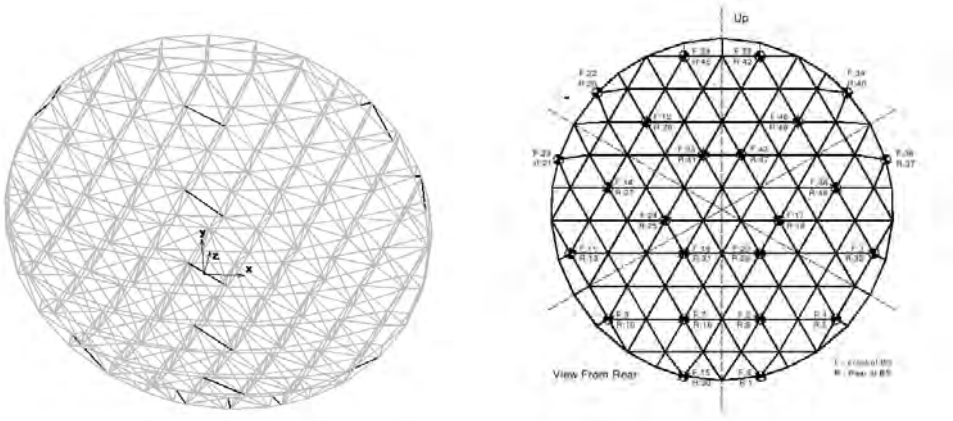

(a) Model of Backing Structure (b) Location of thermistors

Figure 2.3: Model of the backing structure used in the FEA calculations for the OVRO telescope as well as the location of the thermistors. The dark struts are ones which break the lateral symmetry of the dish (Lamb and Woody, 1998)

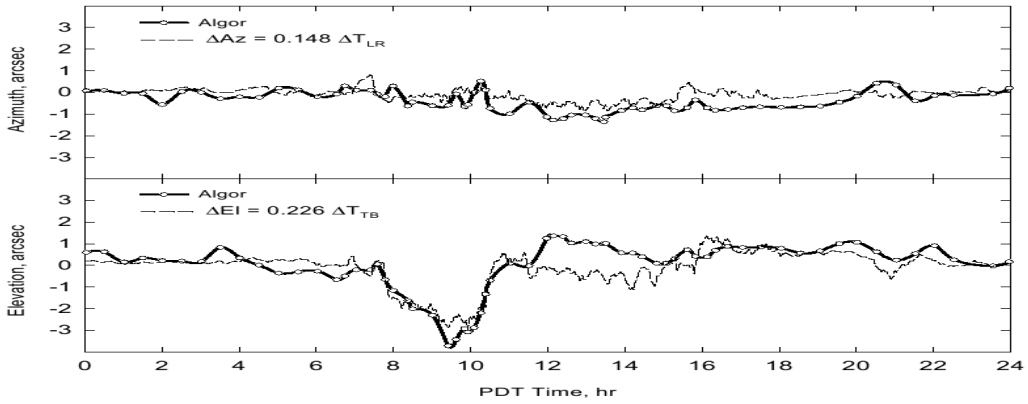

Figure 2.4: Comparison between the full FEA prediction for the pointing offset and an estimate based on a linear dependence on the temperature gradient (Lamb and Woody, 2002).

2.4 The 45 m Nobeyama Telescope

Ukita (1999) deals extensively with the pointing model of the 45 m Nobeyama telescope in Japan, which uses 16 parameters. This model takes into account well understood pointing offset effects such as encoder error, axis misalignments and gravitational deformation and is similar to the VLBI pointing model used at HartRAO. The Nobeyama thermal pointing model was calibrated using sources which had a signal-to-noise ratio larger than 10. A similar criteria was used to separate out poor data in this study of HARTRAO. The paper explored the effect of wind on the pointing and separated data using wind speed as a criteria in certain cases. While wind effects were considered negligible in the HARTRAO study, it is interesting to note that Ukita (1999) estimated that the wind contribution to the pointing offset was

roughly proportional to the square of the wind velocity.

Since the Nobeyama telescope has an ALT-AZ mount, the results were not directly applicable to HartRAO, however they provided insight into the issues. The paper provides a good argument for the importance of good, reliable pointing. The example given is that a pointing error of only 1/5 of the Half Power Beam Width of a Gaussian beam results in a loss of sensitivity of 10 % (Ukita, 1999). This particular telescope operates with a maximum observation frequency of 115 GHz, corresponding to a beam width of 15 arcseconds (or $\approx$ 4.1 mdeg). This makes it necessary to reduce errors to below 0.83 mdeg to maintain a loss of sensitivity of less than 10 %. For HARTRAO, the high end is 22 GHz and the dish is smaller so we would expect a less challenging pointing requirement since the beamwidth would be larger. The 2.5 cm receiver has an estimated beamwidth of 80 mdeg (or $\approx$ 290 arcseconds) so we would require the pointing errors to be below 16 mdeg to avoid a loss of sensitivity of more than 10 %. The 1.3 cm (22 GHz) receiver, with a HPBW of 40 mdeg, would need slightly better pointing still (<8 mdeg) to avoid the 10 % loss of efficiency. Subsection 1.2.1 mentions that the generally acceptable pointing offset is 1/10th of the beamwidth. For the new 22 GHz receiver, this dictates that the pointing offset at HARTRAO be less than 4 mdeg.

2.5 Conclusions for the HartRAO Study

There is general consensus amongst the case studies that the best method for examining pointing offsets is FEA. This provides a solid, physical foundation to studies and future improvements in temperature measurements can easily be added to the model. An FEA model would also allow for other effects such as wind loading to be incorporated at a later stage should this prove necessary.

However, in the case of HartRAO, FEA would be difficult to implement, given the lack of structural diagrams. It would be possible to do a laser scan of the structure (which could be used for FEA), however this would be costly.

An alternative, as suggested by the MERLIN and Leighton case studies, is a very simplified physical model using temperatures from important supports. These case studies suggest that using FEA may not have any significant advantage over this method provided the positioning of the thermistors is carefully considered. Since we were not able to carry out a FEA on the HartRAO structure we focused on investigating the effectiveness of simple models as a starting point.

Chapter 3

Modelling the Problem

This chapter provides general descriptions of the modelling techniques used in this investigation. A brief summary of Finite Element Analysis is included, despite not being used in this study, since the technique is used in the majority of studies in the scientific literature.

3.1 VLBI Pointing Model

A thorough description of the physical effects modelled by the VLBI Model is provided in Appendix B. The VLBI pointing model is parameter based and has the form shown below.

$$\begin{aligned}\Delta X &= P_1 - P_2\cos\phi\sin X\sec Y + P_3\tan Y - P_4\sec Y + P_5\sin X\tan Y \\ &\quad -P_6\cos X\tan Y + P_{12}X + P_{13}\cos X + P_{14}\sin X + P_{15}\cos 2X \\ &\quad +P_{16}\sin 2X \qquad (3.1)\\ \Delta Y &= P_5\cos X + P_6\sin X + P_7 - P_8(\cos\phi\cos X\sin Y - \sin\phi\cos Y) \\ &\quad +P_9Y + P_{10}\cos Y + P_{11}\sin Y \qquad (3.2)\end{aligned}$$

where X and Y represent the Hour Angle and Declination respectively.

Each term models a different pointing effects such as gravitational deformations, axial misalignments, encoders offsets and other static causes of pointing offsets.

3.2 Thermal Expansion

A fundamental relationship that is needed for a physical model of the structure, is how metal expands under different thermal loads. This is given by

$$\alpha_{Steel} = \frac{1}{l}\frac{dl}{dT} \qquad (3.3)$$

where l is the length of the metal.

The fractional expansion of metal is thus related to the temperature difference (dT) through the expansion coefficient α. The equation can be rearranged into

$$dl = \alpha_{Steel} \times dT \times l \tag{3.4}$$

3.3 Simple Physical Model of the Declination Supports

I decided that a simple model would be worthwile after reading a technical report of the Greenbank Telescope (Condon and Constantikes, 2003) where a simple isosceles triangle model is used to predict the approximate magnitude of the pointing errors. This required dimensions of the support structure itself. Unfortunately these were no longer available at the observatory, and previous attempts to obtain blueprints had proved unsuccessful.

I decided that the best way of proceeding would be to get rough dimensions by taking photographs of the structure together with a 1 m ruler for perspective and distance estimates. The photographs were taken by raising ourselves up on the cherry picker to (roughly) the same height as the dish (as determined by a builders level) and obtaining photographs from the North, South and West of the dish with the 1 metre measuring stick in each of the photographs. These photographs (from the various orthogonal views) and the 1 m ruler were then used determine angles and lengths of the various beams in question. A selection of the photographs is shown in Figure 1.1a, 1.1b and 1.1c.

It is immediately obvious that the measurements will be strongly influenced by human perspective as it is difficult to judge accurately from a photograph where a joint ends. For certain beams it is possible to obtain dimensions from the North view and to compare them with similar measurements from the West view. These independent measurements did agree to within approximately 25 cm, however this required careful examination to correlate joints between the two photographs. The estimated dimensions are included in Table 3.1 and simple structural drawings of the structure are shown in Figure 3.1.

Table 3.1: Dimensions of the HARTRAO support structure relevent to the simple physical model. α_{Steel} is the expansion coefficient of steel.

Dimension	Value
l_{North}	8.9m
l_{South}	7.5m
c	1.2m
α_{Steel}	1.2 $\times 10^{-5}$m.K^{-1}

Examination of Figure 3.1c and using Equation 3.4 leads us to Equation 3.5 and

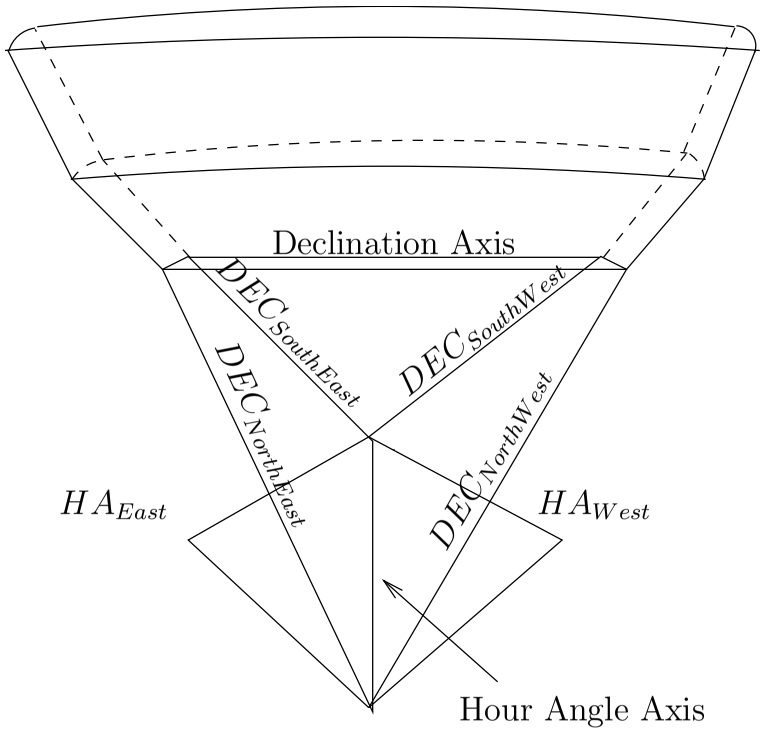

(a) A simplified structural diagram of the axis supports at the HartRAO telescope

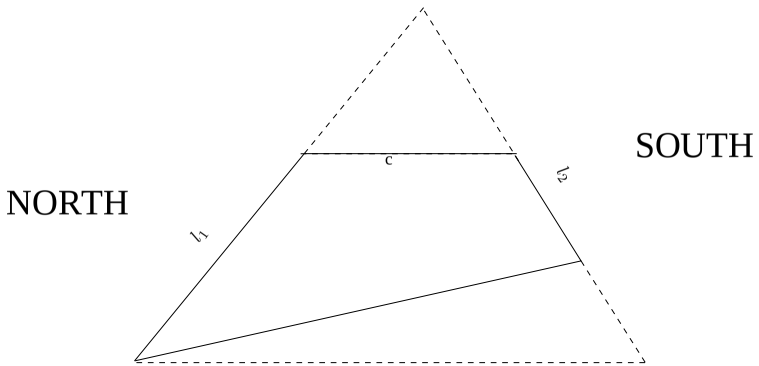

(b) Simplified Declination support structure.

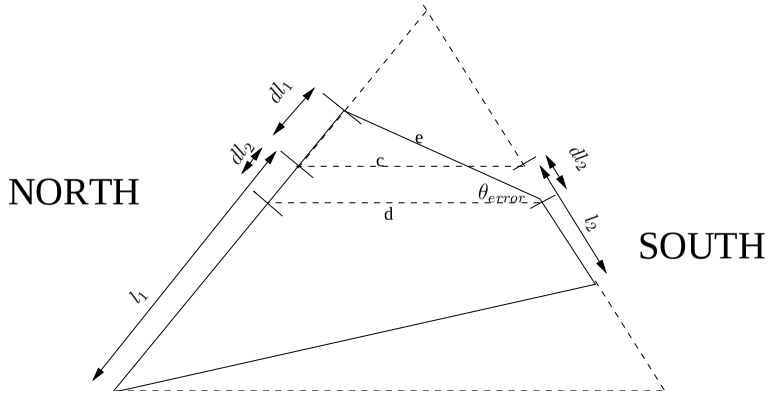

(c) Simplified bending of the Declination support structure. This shows the effect of thermal expansions and contractions along the Declination axis supports, and how these would cause a Declination pointing offset in this simple example.

Figure 3.1: Structural models of the HartRAO Telescope

Equation 3.6.

$$dl_1 = \alpha_{Steel} \times dT_1 \times l_1 \tag{3.5}$$

$$dl_2 = \alpha_{Steel} \times dT_2 \times l_2 \tag{3.6}$$

1. l_1 and l_2 are the lengths of the support beams on either side
2. dT_1 and dT_2 are the difference in temperature of the support beams from the standard reference temperature i.e T_1- T_{ref} and T_2- T_{ref}
3. dl_1 and dl_2 are the relative expansion/contraction of the beams relative to their state at the standard temperature.

On examining Figure 3.1c we see that for small angles (such as those expected here) the following approximation is valid (provided $c \approx d \approx e$)

$$\theta_{error} = \frac{dl_1 + dl_2}{c} \tag{3.7}$$

We can use Equation 3.7 (together with Equation 3.5, Equation 3.6 and Table 3.1) to create a simple model of the Declination pointing offset.

3.4 Correlation Coefficients

Correlation coefficients are a measure of the degree of correlation between two variables, calculated using the following equation (Kurtz, 1991)

$$R = \frac{N \sum xy - \sum x \sum y}{\sqrt{[N \sum x^2 - (\sum x)^2]\,[N \sum y^2 - (\sum y)^2]}} \tag{3.8}$$

This equation produces a value in the interval $(-1, +1)$. A value of $+1$ indicates a perfect positive linear relationship between the variables and a value of -1 indicates a perfect negative linear relationship between the variables. A value of 0 indicates that there is no correlation between the variables.

If there are M variables, an $M \times M$ correlation matrix can be produced made up of the correlation coefficients of the M variables. Element R_{ij} of the matrix is the correlation coefficient between variable i and variable j. The correlation coefficient between a variable and itself will be 1 (since it is a perfect positive linear relationship) and thus the diagonal of a correlation matrix contains only 1's.

Typically, $R > 0.5$ (or $R < -0.5$) shows a good correlation, although this depends on the instrumentation used to collect the data, with higher correlation coefficients expected from higher precision instrumentation.

Correlation matrices are often used as a starting point to investigating relationships between variables. The related covariance matrix serves as a basis for other statistical techniques such as *Principal Component Analysis* and *Factor Analysis*. These techniques can be used to reduce the number of variables to a new set of variables that still contain most of the information.

3.5 Principal Component Analysis

Principal Component Analysis (PCA) is used as a method of reducing a data set to a lower dimension (Schlens, 2005). This is often used to reveal underlying relationships between sets of variables.

A full description of the mathematics behind PCA is not relevent to this study, and is readily available in the literature (Joliffe, 2002; Schlens, 2005), however I will provide a brief summary. PCA takes observations of a set of variables (expressed in a vector space) and changes the basis of this vector space. The new basis is chosen so as to minimise noise by maximising the *Signal to Noise Ratio* (SNR) and to minimise the data redundancy.

The *variance* is defined as (Schlens, 2005)

$$\sigma_A^2 =< a_i a_i >_i \tag{3.9}$$

where $<>_i$ denotes the average of the values over the i indexed values. The variance relates to the SNR.

The *covariance* between A and B is given by (Schlens, 2005)

$$\sigma_{AB}^2 =< a_i b_i >_i \tag{3.10}$$

with high values indicating high redundancy between variables. An important result from the definition of covariance is that $\sigma_{AB}^2 \geq 0$ and $\sigma_{AB}^2 = 0$ only when there is no correlation between the variables.

The *covariance matrix* is a square symmetric matrix where the diagonal terms are the variance of the variables, and the off-diagonal terms are the covariance between the variables. It is used as a starting point for many statistical investigations (including the correlation matrix described in Section 3.4). We can define the covariance matrix of the data as C_X. As mentioned previously, PCA seeks to find a new basis so as to maximise the SNR (maximise the variance σ_A^2) and to minimise the data redundancy (minimise the covariance σ_{AB}^2). A correlation matrix (C_Y) constructed from a perfectly optimised data set would therefore show zero covariance (since zero is the minimum achievable covariance) between variables and therefore the off-diagonal terms of C_Y would be zero. This is the definition of a diagonal

matrix, and minimising the covariance can then be redefined to the problem of diagonalising C_X.

PCA assumes that all basis vectors $(p_1, ..., p_m)$ are orthonormal (i.e $p_i.p_j = \delta_{ij}$) and thus that the matrix P is orthonormal. PCA secondly assumes the directions with the greatest variance, which maximises the SNR for reasons outlined earlier. The algorithm used by PCA is as follows

1. Select a direction in the m-dimensional space along which the variance of the variables is maximised. This is saved as P_1, the first principal component
2. Find another direction along which the variance is maximised, however this direction should be perpendicular to the first direction due to the requirement of orthonormality
3. Repeat this process until the m vectors are completed

From the above it is important to notice the following restrictions on PCA

- PCA will only reveal linear relationships between variables
- The Principal Components are orthonormal
- The Principal Components will be ordered in decreasing variance

3.6 Linear Fitting of Weighted Inputs

Simple models for a phenomenon can be constructed if the cause is thought to be understood. In the case of the HartRAO pointing offset, we suspect that differential heating of the the axis supports may cause deformations in the supports, resulting in axis movements which cause the pointing offsets.

If temperatures of the axis supports are given by $AT_1, ...AT_n$, then a simple model involves assigning variable weights to these temperatures and adding these weighted temperatures.

$$\text{Model Pointing Offset} = \sum_{i=1}^{i=n} a_i AT_i \tag{3.11}$$

A suitable fitting technique can be used to obtain the best-fit weighting vector a_i. If the support temperatures do play a role in causing pointing offset, this would produce a model of the pointing offset which uses the support temperatures as inputs.

This method is often recommended as a replacement for FEA (see Section 3.8) when the complexity of FEA is not justified or when FEA is difficult to implement, as is the case at HartRAO.

3.7 Neural Networks

Neural Networks are loosely derived from biological systems, with the system being defined by the relationships between all the elements (MATLAB R14). They have certain advantages over other modelling systems in that non-linear effects are easily taken into account, the development of the model is relatively quick, and a thorough physical understanding of the entire system is unnecessary. All that is required to roughly model the HartRAO pointing offset using neural networks, are pointing offset measurements and corresponding axis support temperatures. The disadvantage is that since little physical understanding is required, any physical change in the structure requires the model to be retrained. This should not be a significant disadvantage when compared against most other methods, apart from a Finite Element Analysis (see Section 3.8) of the structure. A further disadvantage associated with the lack of physical understanding is the danger of complete

The fundamental building block of a neural network is the neuron which is introduced in Figure 3.3a. As shown in Figure 3.3a, a scalar input, p, is multiplied by a weighting matrix and a bias is added. This is then used as the argument to a transfer function. A number of different transfer functions can be utilised depending on the application and the training method. MATLAB provides a wide variety but as an introduction, shows the transfer functions in Figure 3.2.

A typical neural network will involve an input matrix, a neural network consisting of one or more neurons as well as possibly more than one layer of neurons, and the corresponding output vector.

In the simplest case, the output of the transfer function is fitted to observations (using non-linear fitting techniques) by changing the weighting matrix. More complicated systems may involve using more neurons before the output as in Figure 3.3e. The actual fitting occurs through a minimisation of the difference between predicted and observed errors as shown in Figure 3.3b.

3.7.1 Overfitting

One of the potential problems associated with neural networks is *overfitting*. This results in the neural network fitting extremely well to the training data set, but not when applied to to new (unseen) data.

Two major techniques are used to overcome this problem (Doan and Liong; The Mathworks, 2005). These are

1. Early stopping method

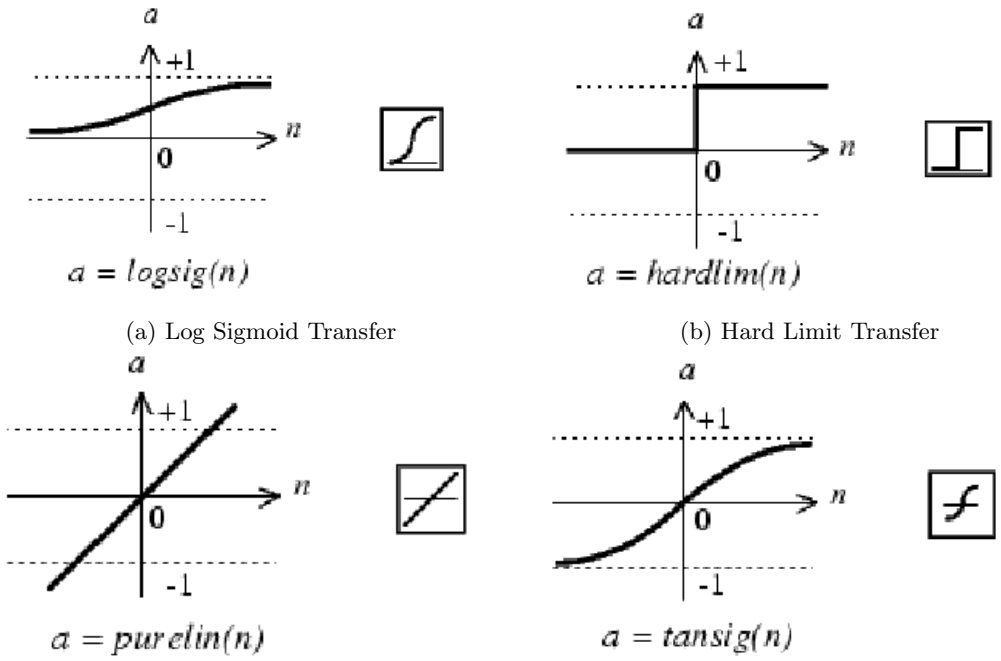

(a) Log Sigmoid Transfer

(b) Hard Limit Transfer

(c) Linear Transfer

(d) Tan-Sigmoid Transfer

Figure 3.2: Different transfer functions used in neural networks (MATLAB R14)

2. Bayesian Regularisation

The early stopping method was employed in this data analysis. This requires that the data be divided into 3 sets. These are known as the Validation, Testing and Training sets respectively. The neural network is trained on the Training set and updates the weights and biases. The neural network monitors the error between the model predictions and observations for the Validation set throughout the training. In the beginning of the training, the error will decrease as the fitting improves. When the network begins to overfit to the Training data however, the Validation set error will typically begin to rise. If this occurs for a specified number of training iterations then the training is stopped.

The Testing data set is not used in the process but its error can be compared to the error of the Validation training set. If the data has been divided poorly, the two errors will not be consistent with each other. This can be remedied by redividing the data to contain evenly spread points across all the sets.

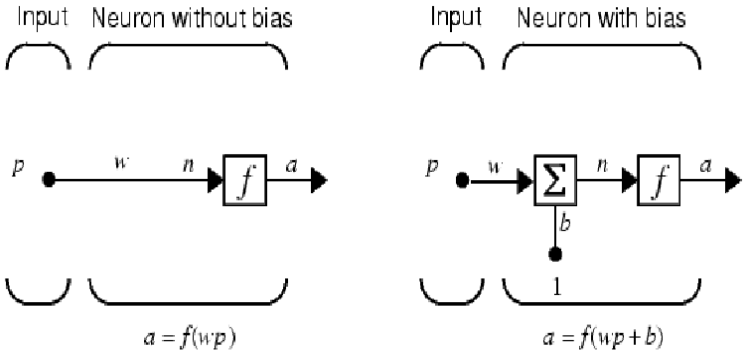

(a) The figure on the left shows one without bias input while the one on the right includes bias input.

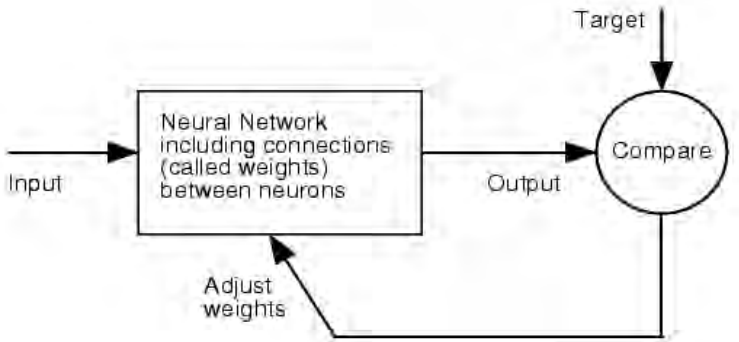

(b) Depiction of neural network training method. This shows the feedback of the output and the minimisation routine.

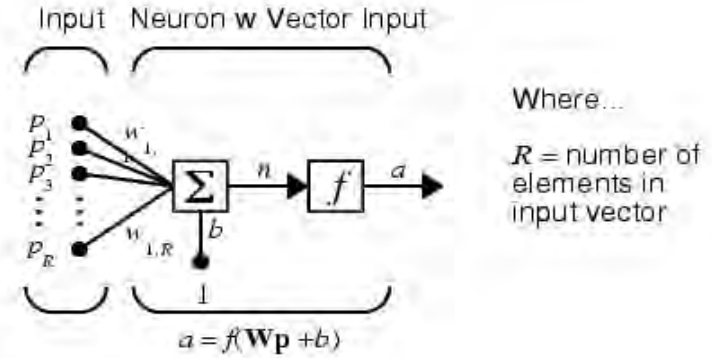

(c) An input vector being used as the input to a neuron.

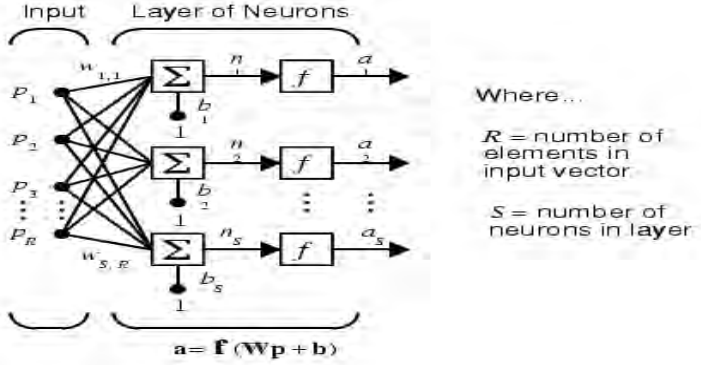

(d) A one layer neuron neural network

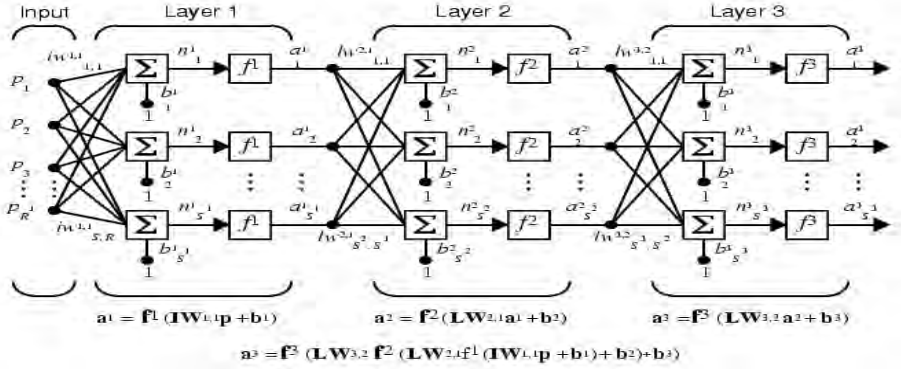

(e) A multi layer neuron neural network

Figure 3.3: Diagrammatic examples of neural network nomenclature and structures (MATLAB R14).

3.8 Finite Element Analysis

Finite Element Analysis is the primary tool used in the majority of thermal correction models. The idea is that the antenna can be represented by linked elements, each of which has an associated set of equations. Examples of these elements include triangles, hexagons, cubes etc.. The finite element procedure involves three steps:

- Pre-processing
- Solving
- Post-processing

In pre-processing the finite element model is constructed. This model should replicate the important parameters of the antenna, such as material and structure, and is generally obtained from existing blueprints.

A meshing procedure is then applied, where the model is broken up into smaller constituent elements, each with their own associated set of equations. Nodes are then defined as positions of important points on these elements, and are used to calculate displacements and other useful features of the model. Constraints are then placed on particular nodes to simulate the real model more accurately. Certain nodes may, for example, have movement restricted in certain axes to simulate fixed points on the structure.

The solving step follows. External loads, such as forces, temperatures, pressures etc. are applied to the finite element model and resulting displacements of nodes are then iteratively updated. This iterative process continues until a minimum output is reached and the nodes are consistent within themselves. The final displacements are then noted.

Post-processing is then applied to the resulting displaced nodes. This allows the user to visualise the effects of the initial loads placed on the model. In the case of thermal deformations of an antenna, it would be possible to place a set of temperature loads on the model, and then to visually inspect the effect this would have on the structure as a whole.

This study does not use FEA primarily due to a lack of accurate telescope dimensions. I did investigate various options to obtain the necessary dimensions using measurement techniques. Prof. Heinz Ruther of the University of Cape Town Geomatics Department suggests that the most suitable technique would be to use a laser-scanner. This would allow dimensions accurate to 6mm RMS to be obtained, but would be expensive to implement.

At this stage I decided not to pursue this option further as the HartRAO pointing requirements could probably be satisfied with a less sophisticated model which would be easier and less expensive to realise.

3.9 Summary

This chapter describes different techniques relevent to modelling pointing offsets in radio telescopes. Of particular importance to this study are the simple models of the telescope support structure and the implications that the dimensions of the supports have on pointing offsets assuming thermal expansion of the supports.

An overview of the theory behind correlation matrices and Principal Component Analysis, which are of importance to modelling in general, is included. These concepts are used in analysing the data in Chapter 5. Description of the linear weighting model, as well as justification for its use is included and a theoretical background of neural networks explains the usefulness of this modelling technique to the problem of pointing offsets as well as describing the possible dangers in using this method.

The chapter concludes with a brief overview of the FEA process, primarily because of its ubiquitous use in similar studies.

Chapter 4

Data Capture and Reduction

The calibration of pointing models requires the observation of the position of a catalogue of strong point sources.

This chapter describes the instrumentation used during these observations and outlines the experimental design. It includes a description of how pointing offsets were obtained by fitting different beam profile functions to point source scan data. I outline the layout of the code that reduces the observations to pointing offset measurements and explain how data quality is ensured. I conclude the chapter by including the resulting pointing offsets and describing the refitting of the VLBI pointing model using these new results.

4.1 The HartRAO Antenna

The Hartebeeshoek Radio Astronomy Observatory (HartRAO) dish is located 80 km west of Johannesburg, South Africa. It was initially built by NASA as a tracking station for probes sent beyond the Earth's orbit. The initial surface was made of aluminium mesh and operated at a frequency of 960 MHz (30 cm). In the mid-1960's the surface was upgraded to aluminium panels, and the frequency changed to 2300 MHz (13 cm). The antenna was handed over to the South African government in 1974, and was transformed into a radio telescope. Subsequent upgrades of receiver systems and dish surface, have led to the current configuration with receiver systems at 18 cm, 13 cm, 6 cm, 5 cm, 4.5 cm, 3.5 cm, 2.5 cm and 1.3 cm.

The dish has an equatorial mount, and features a Cassegrain optical system with a 25.9 m parabolic primary reflector. The receiver feeds are mounted in a feed cabin on the primary reflector, close to the optical axis of the secondary reflector.

4.2 Telescope Control

The automatic observation system at HartRAO accepts a list of objects for a particular observation schedule. The objects are typically entered together with their J2000 (or B1950)

mean coordinates and observation strategy, and the observations are given a priority rating. It was anticipated that we would need to experiment with this priority rating in order to obtain sufficient observations without 'locking' other observations out of the scheduler. Fortunately this did not materialise as an issue.

An example of a typical object input to the observation file is given in Listing 4.1. This is an extract from *pointing.cat*. The keywords defined in the catalogue are referenced in the scheduler file (included in Listing 4.2) which sets up other observation properties such as wavelength, start and end time and the type of scan. The HartRAO website (HARTRAO, b) includes more information on different setup options.

```
OBJECT  0023-26, B0023-263
// Good for pointing at X-band, but weakish
COORDSYS  EQUATORIAL
EQUINOX   1950.0
RA        00 23 18.914
DEC      -26 18 49.25   // VLA
ENDOBJ
```

Listing 4.1: Typical Observation object in the observation catalogue *pointing.cat*. The layout is self-explanatory, defining the coordinate system and equinox used as well as the position of the source in the defined equinox. It specifies a keyword (0023-26) used by the scheduler file (see Listing 4.2) to identify which objects will be included in observations

```
 SETUP
OBSERVER  Jonathan Quick                  //observer name
PROJECT   Refining the New Pointing Model using X-band //project ↘
title
PROPOSAL  2005.99                                 //proposal number
OBSLOCAL  jon                                             //local ↘
observed username
STRTDATE  2006 07 18             //date on which observations should ↘
start
STRTTIME  00 00 00.0             //time at which observations begin
ENDDATE   2007 12 31             //date on which observations end
ENDTIME   00 00 00.0             //time at which observations end
CATALOG   pointing.cat  //reference to the catalogue containing ↘
objects that should be observed
PRIORITY  FOREGROUND    //priority level of the survey
ORDER     RANDOM                          //order of observations ↘
through the catalogue
OUTFILE   Copley
CONF 3.5CM                                                //observation↘
 wavelength
RESTFREQ  8400.000E6
INSTRUME  DICKE                           //Dicke switching to remove ↘
atmospheric contaminations
SCANTYPE  CROSSED                         //Cross scan observation
SCANDIST  SN
SCANS     8
SCANANGL  0.0
ALTLIMIT        60.0             //angular elevation above which ↘
observations are made
```

```
WEATHER          CLEAR            //worst allowable weather conditions ↘
during which observations are made
ENDCONF
ENDSETUP

// Good for pointing at X-band
OBJECT  0316+41 // aka 3C84
USECONF 3.5CM
ENDOBJ
.....
```

Listing 4.2: Typical scheduler file used during these observations. This sets the observation wavelength, dates, objects and other conditions related to the observations. Important to note is the ALTLIMIT keyword which specifies that observations will only be made at elevations greater than 60°. This means that all observation will be within 30° of zenith minimising other pointing offset effects such as gravitational deformation. We limit observations to only occur during clear weather conditions. Keywords of objects to be used from the pointing catalogue are included below the ENDSETUP keyword- in this example only 0316+41 would be used. Further details are available on the HartRAO website (HARTRAO, b)

In the scheduler input file shown in Listing 4.2 we see that the observation file is *pointing.cat* and the priority is given as *FOREGROUND*. We see the the scantype is defined as *CROSSED* and that Dicke Switching is being utilised.

4.3 Experiment Design

4.3.1 3.5 cm Receiver

The pointing observations were conducted using the 3.5 cm receiver. This receiver has a dual feed which permits Dicke-switched radiometry. I have concentrated on the left circularly polarised feed in this investigation.

4.3.2 Thermistors

Temperature was recorded using the AD592 IC. These IC's provide a current which is proportional to the absolute temperature. These have an accuracy of 0.5°C at 25°C (Analog Devices, a). Two were mounted on each of the four primary Declination axis supports at two different places approximately 2 m apart and at approximately the same position on each support. One thermocouple was mounted on each of the Hour Angle supports. The exact positions were not considered to be important at this stage.

The SCADA data collection unit recorded temperature readings every 1 minute for all ten of the IC's.

4.3.3 Description of Observations

The type of observations used are described by the *CROSSED* keyword in the observation file. A total of 4 scans along each axis are made for each observation to give a total of 8 scans per object. For each scan, coordinates are recorded in a multitude of systems. Each scan comprises 460 signal samples, with the associated time/position. These 8 scans are stored in a FITS file, a file format commonly used for astronomical observations.

During each scan one of the coordinates is kept fixed, while the other is varied to produce a cross-scan of the object. This is shown in Figure 4.1a. I have included the Right Ascension scan and the Declination scans separately in Figure 4.1b and Figure 4.1c, to highlight the difference in the movement between the two scans.

Hour Angle and Right Ascension are related through sidereal time. The local coordinate system of the HartRAO antenna is the Equatorial Hour Angle and Declination. To maintain a fixed Right Ascension position the antenna is forced to move through Hour Angle as the sidereal time changes. This leads to inevitable drifts while attempting to keep the Right Ascension position fixed. We see the slight drift in the Right Ascension in 4.1b. For the Right Ascension scan the antenna does not need to move to maintain a fixed the Declination. The changes in Declination that we see in 4.1c are only quantisation errors of the encoder.

As each scan is completed the coordinates of the maximum signal are recorded and used for the following scan so that the telescope can 'centre in' on the observed object and obtain a maximum signal. This overcomes the problem that the the initial scan is often not on the source. I have effectively treated the first scan along each axis as a 'calibration' observation as a result.

In the initial stages of the reduction program development I only used Scan 4 since this should be on-source. I was flagging data manually at that stage and dealing with the additional scans would have been difficult. I subsequently increased the scope to include Scan 2,3 and 4 along each axis by imposing a set of criteria outlined in Section 4.7. This set of criteria simplified the automatic flagging procedure considerably and allowed me to fit elliptical Gaussians rather than quadratics (see Section 4.4).

4.3.4 Choice of observed object

Our typical observation requires that the object conform to the following specifications:

- Strong point source
- Close to Zenith during observation (to minimise gravitational and atmospheric effects on the pointing)

- Accurately known mean position

Fortunately the observation scheduler (which is outlined in Section 4.2) allows constraints to be placed on a list of suitable objects. These constraints included zenith distance which allowed a limit to be easily placed on the zenith distance. A suitable zenith distance of 30 ° was decided on. This prevented observation of any objects not within 30 ° of zenith. We removed any objects not within the range of 5 ° → -55 ° Declination as they would never pass within the required distance of the zenith (since HartRAO is at approximately 25 ° South latitude). We only used bright sources with mean positions determined by VLBI measurements.

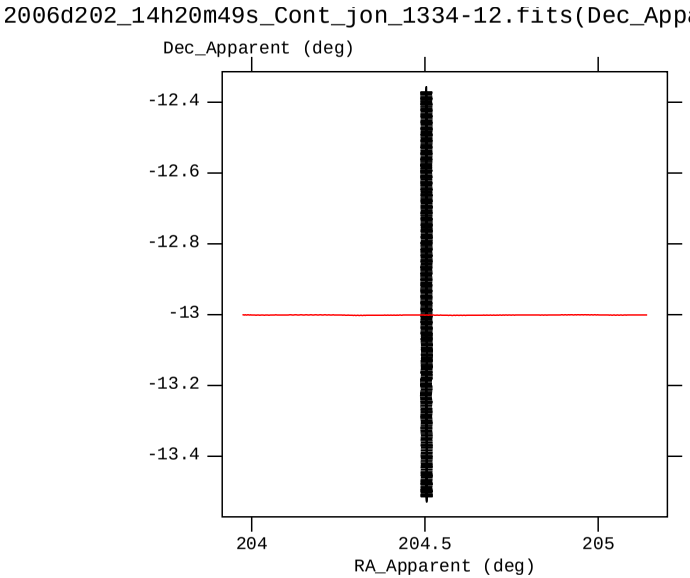

(a) Both Scans plotted together

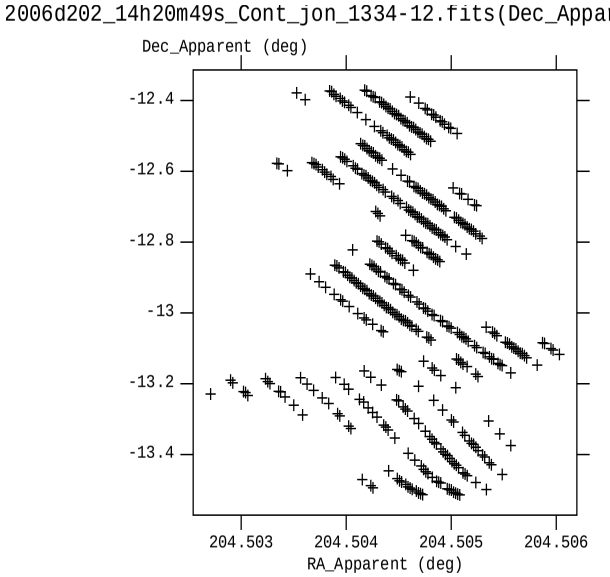

(b) Declination scan showing the effect that changing sidereal time has on maintaining a constant Right Ascension through the scan.

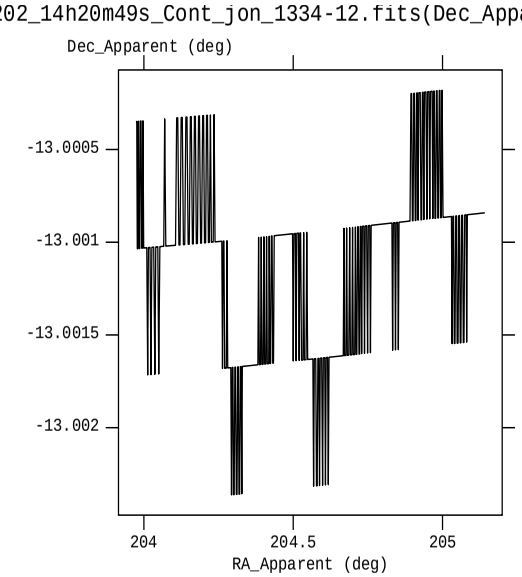

(c) Right Ascension scan showing the effect that encoder quantisation errors have on maintaining a constant Declination through the scan.

Figure 4.1: A typical cross scan trajectory of an object showing the Right Ascension and Declination movement of the telescope beam.

4.4 Measuring Pointing Offsets Using Point Sources

This section describes data obtained at HartRAO from point source observations, and introduces analytical functions that can be used to obtain the observed position from the observed signal distribution. Pointing offsets can be obtained by comparing the observed position of a point source against an accurately known VLBI catalogue position.

4.4.1 Typical Data from Point Source Observations

Data typical of a cross scan of a point source is included in Figure 4.2. Observations require baseline correction as illustrated by Figure 4.2. It is used to remove any slope or offset in the baseline due to atmospheric/electrical changes or variations of the response of the antenna during the scan. In these examples a quadratic baseline is fitted using the first and last 50 data points in the scan and is then subtracted from the data. The *baseline corrected* data is shown in Figure 4.3.

There is a noticeable difference between the two cross scans, with the Declination scans only showing one negative peak and the Right Ascension scans showing both a negative and positive peak. The negative peak occurs due to the beam differencing operation of the dual-beam dicke switched radiometer. The positive peak in the Right Ascension cross scan is due to the Hour Angle movement of the dual-beam *across* the point source. Declination cross scans do not result in the both beams moving across the point source and only show the negative peak.

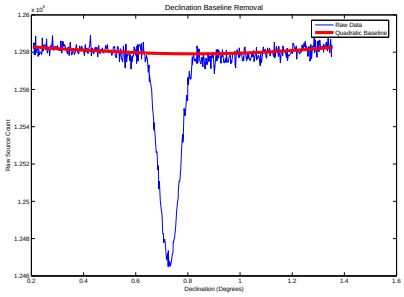

(a) Typical Declination Cross Scan

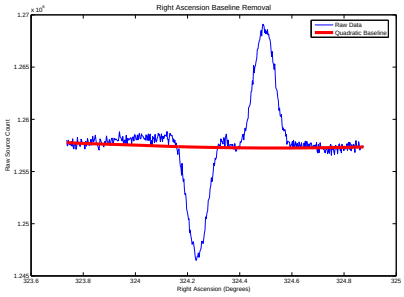

(b) Typical Right Ascension Cross Scan

Figure 4.2: Typical Raw Data from a Set of Cross Scans

4.4.2 Elliptical Gaussians

The main beam lobe of a radio telescope can be approximated by an elliptical Gaussian distribution given by Equation 4.1

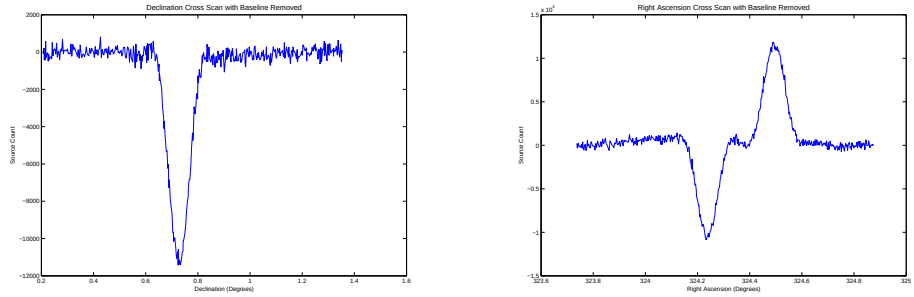

(a) Typical Declination Cross Scan

(b) Typical Right Ascension Cross Scan

Figure 4.3: Typical Data from a Set of Cross Scans with Baselines Removed

$$T_{source}(x,y) = A_1 exp\left[-\frac{(x-x_0)^2}{2\sigma_x^2} - \frac{\beta(x-x_0)(y-y_0)}{\sigma_x\sigma_y} - \frac{(y-y_0)^2}{2\sigma_y^2}\right] \tag{4.1}$$

An observation of a point source will result in a signal distribution given by Equation 4.1. Combining the cross scans and fitting an elliptical Gaussian to the signal distribution, as shown in Figure 4.4 and Figure 4.5, allows the position of the point source to be obtained. If the object's celestial coordinates are accurately known from VLBI measurements, these observed positions can be used to obtain pointing offsets.

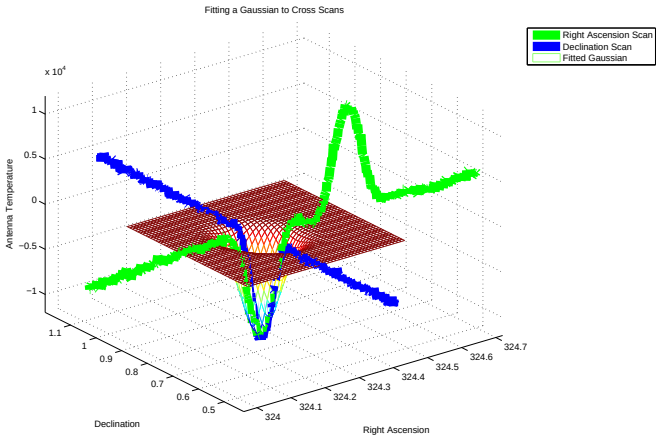

Figure 4.4: An elliptical Gaussian fitted to the combined Right Ascension and Declination data

In the final data reduction I combined the Declination and Right Ascension cross scans introduced in Subsection 4.4.1 and fitted an elliptical Gaussian to this combined data. The second Declination scan was combined with the second Right Ascension scan and a Gaussian was fitted to this combined data. I continued by using the third Declination and Right Ascension scans to fit a second Gaussian and did the same with the fourth Declination and Right Ascension scans to produce a third Gaussian fit. I did not use the first scan for reasons

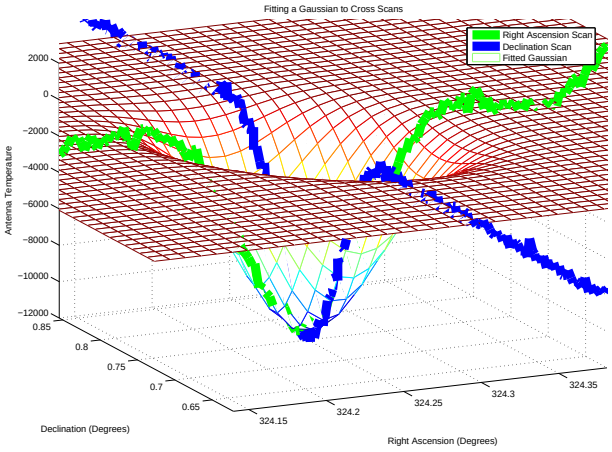

Figure 4.5: A closer view of the elliptical Gaussian shown in Figure 4.4

outlined in Subsection 4.3.3.

Elliptical Gaussian Uncertainties

Estimating uncertainties for the observation parameters is not trivial. Condon (1997) explains a general method for estimation used when fitting an elliptical Gaussian to images and estimating uncertainties in terms of pixels. In this case I used the following common astronomical definitions

$$\Theta_M = \sqrt{8ln2}\sigma_x \tag{4.2a}$$

$$\Theta_m = \sqrt{8ln2}\sigma_y \tag{4.2b}$$

$$\rho^2 = \frac{\pi}{8ln2}\frac{\Theta_M \Theta_m A^2}{h^2 \mu^2} \tag{4.2c}$$

The error estimates of these values are given by

$$\frac{2}{\rho^2} \approx \frac{\mu^2(A)}{A^2} \tag{4.3a}$$

$$= 8\ln 2 \frac{\mu^2(x_0)}{\Theta_M^2} \tag{4.3b}$$

$$= 8\ln 2 \frac{\mu^2(y_0)}{\Theta_m^2} \tag{4.3c}$$

$$= \frac{\mu^2(\Theta_M)}{\Theta_M^2} \tag{4.3d}$$

$$= \frac{\mu^2(\Theta_m)}{\Theta_m^2} \tag{4.3e}$$

A note here is that the h^2 represents the area of each 'pixel' and the μ represents the RMS of the noise in the scan. To use this method, I estimated the RMS as the RMS of the first 50

data points in both the Declination and Right Ascension scans. I estimated the 'area' of each pixel (in square radians) by multiplying the Declination step size by the Right Ascension step size. An explanation of the derivation of the equations given in Equations 4.3 is included in Appendix A. I found the estimated uncertainties in position estimated from the Gaussian fitting to be negligible ($\ll$ 1mdeg) compared to the desired pointing accuracy of approximately 4 mdeg, and so I haven't focused much attention on them in this study. Typical values are included in Appendix A.2, Figure A.1a and Figure A.1b to substantiate this decision.

4.4.3 Other Functions

Simpler functions such as 2-D Gaussians or quadratics are often used instead of the elliptical Gaussian to obtain the observed position. This is because it can prove difficult to automate the fitting process of the elliptical Gaussian due to the complexity and non-linearity of the function.

2-D Circular Gaussian

It is often computationally easier to fit a 2-D Gaussian to a signal, and to use this to obtain positions of objects from pointing scans along one axis. A 2-D Gaussian can be expressed as

$$T_{source}(x) = P_i exp\left(-\frac{(x - X_i)^2}{2\sigma_i^2}\right) \tag{4.4}$$

A Gaussian of this form is characterised by 3 parameters. These are the central abscissa X_i, the central ordinate P_i and the dispersion σ_i (Kaper et al., 1966). Uncertainties can be estimated (Kaper et al., 1966; Gaylard, 2005b) such that (where a = Number of Data points across FWHM)

$$\sigma_{P_i} = \left[\frac{RMS_{noise}}{\sqrt{a}}\right] \tag{4.5}$$

$$\sigma_{width} = Width \times \frac{\sigma_{P_i}}{P_i} \tag{4.6}$$

$$\sigma_{X_i} = \frac{\sigma_{width}}{2} \tag{4.7}$$

Quadratics

A quadratic is even less computationally difficult to fit than a 2-D Gaussian. This is often used as a first approximation to the lower quarter of a Gaussian signal, and positions can be estimated from this. For the initial purposes of my investigation, a Gaussian fitting was not required since I was only interested in the position of the peak and I began this study by using a quadratic approximation. This has the advantage of being considerably simpler to implement and more robust than Gaussian fitting since we can work with a linear function.

4.5 A Priori Pointing Corrections

There are three possible corrections that may have been applied to the observed coordinates before they were written to the FITS file. These may need to be removed from the data before data analysis can be done. The pointing corrections are:

1. Refraction
2. VLBI Pointing Model Corrections
3. Dr. Nicolson's original thermal pointing correction model

The first and second of these models was applied to all of the data that I collected, while the third model was only applied to data collected before January 2007, after which a keyword was added to the scheduler file parser (see Listing 4.2) to allow the application of this pointing correction to be selected. The two sets of observations were stored separately and it was easy to note whether the thermal correction model had been applied or not. It is necessary to remove the thermal pointing correction model from the observations before beginning any analysis. Depending on the type of analysis, it may be necessary to remove the VLBI Pointing Model corrections.

4.6 Data Reduction

The data reduction is done in two steps. The first involves extracting the data, pre-processing it and returning initial values of the pointing offset and the second analysing this data and fitting various models to it.

4.6.1 Step One- Extraction and Reduction of Data from Observation FITS Files

I used Fortran77 code primarily because of the availability of the established FITSIO library which allowed easy manipulation and reading of FITS file data.

Code was written to read in data from each FITS file sequentially. The observations contained in the FITS files are detailed in Subsection 4.3.3 and flow charts of the basic process are shown in Figure 4.6. The program first subtracts a baseline from each of the scans (as shown in Figure 4.2) and then proceeds to obtain initial estimates of the Gaussian parameters using a quadratic fit across the Gaussian peak. These estimates are then used to provide reasonable starting values for the non-linear fit of the elliptical Gaussian.

Thereafter the scans are grouped into sets of two comprising a Declination scan and a Right Ascension scan. The data sets are combined and a elliptical Gaussian is fitted to the

combined data with the peak position recorded. The program records whether the thermal correction model has been applied to the data as well as the heuristic thermal correction model value for the time of the scan. It removes the VLBI pointing model from each of the scans and writes the Declination, Right Ascension, Hour Angle and signal counts to file. Uncertainties are estimated for each of fit parameters and then saved to file. The data with the VLBI model removed is used later in refitting the VLBI model (results shown in Figure 4.8), to ensure that there is minimal contamination from other causes of pointing offset besides the thermal effects. The file names containing the data are summarised in Table 4.1.

Table 4.1: Summary of the contents of the *analysis.txt* files output in the first stage of the data analysis.

File	Description
analysis.txt	Primary Data from fitting to the data before removing the VLBI pointing model. Includes time, the catalogue position of the object and whether Dr. Nicolsons original temperature correction had been applied together with the correction that needed to be removed.
analysis1.txt	Further information on the object such as ambient temperature and the epoch used for catalogue positions
analysis2.txt	The Left Circularly Polarised Scans from each FITS file. These are the scans with the VLBI pointing model removed from the coordinates.
analysis3.txt	The Right Circularly Polarised Scans from each FITS file with the VLBI pointing model removed from the coordinates
analysis4.txt	Uncertainty estimates for the Left Circularly Polarised Data fits
analysis5.txt	Uncertainty estimates for the Right Circularly Polarised Data fits

A note should be added to the above. The current system derives all coordinates from apparent Hour Angle and Declination. This is the Hour Angle and Declination once corrections for refraction and diurnal aberration are made. The conversion from Hour Angle to Right Ascension requires the local apparent sidereal time which can be calculated from UT1. UT1 is not the same as UTC and differs from the latter by less than a second at all times (this is maintained by adding and subtracting leap seconds from UTC). The conversion from Hour Angle to Right Ascension at HartRAO ignored this small difference between UT1 and UTC and assumed UT1=UTC in the calculation of the sidereal time. I have compensated for this by retroactively applying a UT1-UTC correction and recalculating the Right Ascension values listed in the FITS files. This change has subsequently been incorporated into the HARTRAO control system.

4.6.2 Step Two- Examining Different Pointing Model Effectiveness

The rest of the data analysis is performed in MATLAB. This is done to take advantage of the greater versatility provided by this high level programming environment. I initially wrote a number of scripts to perform the analysis, however it soon became difficult to keep track of what had been done and I found myself redoing many time consuming calculations far too many times for my sanity. I decided to create a GUI (screenshot shown in Figure 4.7) which allowed previous results to be saved to file and allowed me to keep a better track of what I was doing.

The GUI allows me to proceed easily through the following options:

- Removing thermal pointing corrections if necessary.
- Recalculating VLBI Pointing Model coefficients in an effort to remove any remaining systematic pointing errors .
- Correlating temperature readings with scans. Both instantaneous thermal conditions and an average of temperature readings over a previous period were calculated since temperature effects do not to have an instantaneous effect on the support structures and might occur as a result of earlier temperature conditions.
- Binning data according to thermal properties if necessary.
- Attempting to model the pointing offsets using the models outlined in Chapter 3.

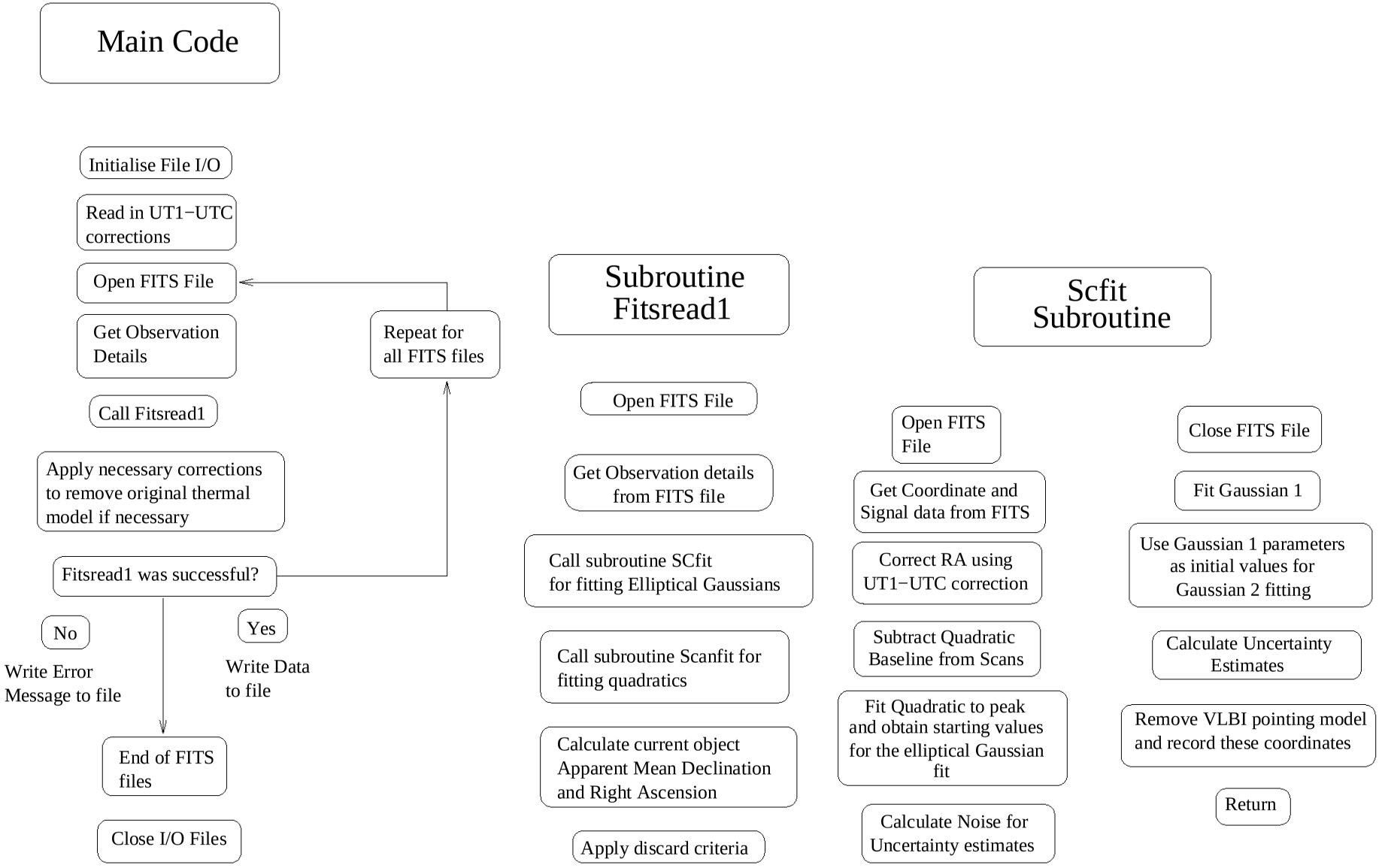

(a) Summary of the operations performed in the main code.

(b)

(c)

Figure 4.6: Flow diagram of the Fits2point Fortran code.

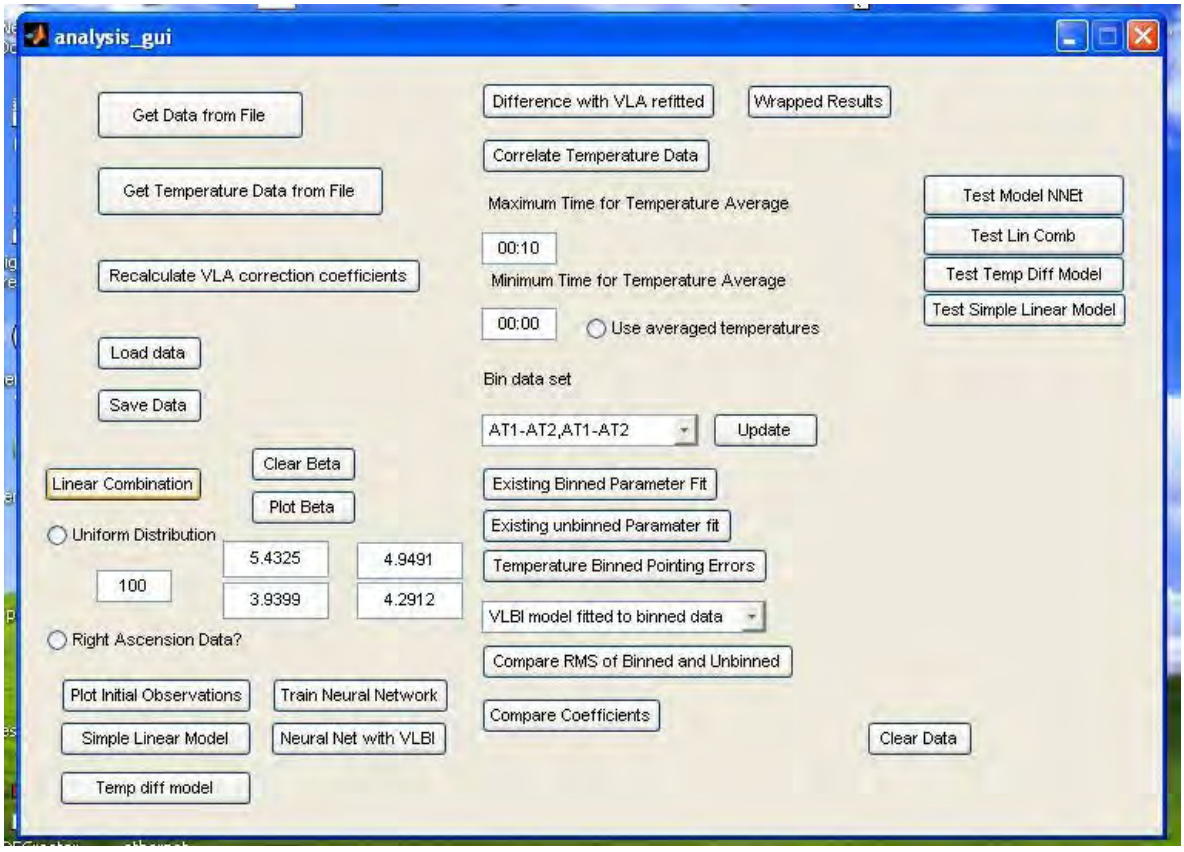

Figure 4.7: Screenshot of the MATLAB GUI interface used for the data analysis

4.7 Ensuring Data Quality

After beginning data collection, it became evident that a relatively large portion of the observations (approximately 10%) were entirely unsuitable for use as pointing offset measurements. Many had low signal to noise ratios and certain scans appeared to have missed the source completely.

In an effort to minimise manual requirements I imposed a set of criteria on the observations which needed to be met before the observation was used in the data reduction. The criteria was similar to that used in Ukita (1999) on the Nobeyama Telescope (see Section 2.4). The selection criteria are given below:

- Signal to noise ratio greater than 10
- Pointing offset of less than 40 mdeg for both axes (estimated from quadratic fitting to the source) to discard obviously faulty scans. This assumed that thermally induced pointing errors were less than 40 mdeg which I believe to be a reasonable assumption since this is the beamwidth size. Any automatically calculated errors larger than this must be as a result of faulty scan data since the object would probably not have been within the beam at all.
- Of the 3 scans used along each axis, at least 2 should give measurements agreeing within 5 mdeg. Any not within this band were discarded. This allowed for one of the scans to be useless without discarding the other two.
- Quadratic fitting should be 'successful' on at least 2 of the scans. This means that the quadratic fitting should provide initial Gaussian parameter estimates for 2 corresponding Declination and Right Ascension scans which are used to fit the Gaussian. The process is explained briefly in Subsection 4.4.2.
- At least 2 out of the possible 3 Gaussian fittings should be successful.

This selection criteria is applied during Stage 1, and works well. Without the criteria a significant number of outlying data points are allowed into the data which require manual removal. Forcing all observations to have a pointing offset of less than 40 mdeg (Criterion 2) has obvious limitations if fitting to questionable scans still produces pointing errors less than 40 mdeg, however I felt that a high signal to noise ratio (Criterion 1) and and agreement between separate scans (Criterion 3) taken together would remove any such untoward observations from the data set.

4.8 Initial Observations and Refitting the VLBI Pointing Model

Data was collected from July 2006 to July 2007 and the pointing offset observations are summarised in Figure 4.8. We would expect that the pointing offsets should centre around (RA,DEC)=(0,0) with scatter due to pointing offset effects not considered in the VLBI pointing model.

As more data was obtained it became increasingly obvious that the pointing offset had an inherent non-zero offset as shown in Figure 4.8. This implies that other sources of pointing offset modelled in the VLBI pointing model may be influencing the pointing offset. Before trying to model the thermal effect on the pointing offsets, these other sources of contamination need to be removed as best as possible. To achieve this I removed the existing VLBI pointing model from observations and then refitted the parameters. The effectiveness of this refitting was potentially compromised by the 30° zenith angle limit (since the pointing model should be fitted with observations from as many different directions as possible), however it would at least allow the pointing offsets to be centred about zero for our purposes. The remaining offset would hopefully be due to effects not included in the model such as thermal effects.

The results of this process are promising, as shown in Figure 4.8. The centroid of the original pointing offsets was at approximately (RA,DEC)=(-15,5) mdeg in the original pointing offset observations. This reflects poorly on the current parameters of the VLBI pointing model. The new coefficients result in reducing the systematic offset and moving the centroid to approximately (RA,DEC)=(0,0) mdeg. The variance of the pointing offsets is only marginally improved. The old and new parameters are shown in Table 4.2

Table 4.2: VLBI Pointing Model Parameters and the results of refitting the parameters using these observations.

Description	Original	Refitted	% Change
P_1	-0.0074075498	-0.01049454780367	29.4153
P_2	-0.0063556978	-0.00686492941186	7.4179
P_3	-0.0047638724	-0.00517999928007	8.0333
P_4	-0.0024362272	-0.00279710700103	12.9019
P_5	0.0544945337	0.05452390127463	0.0539
P_6	-0.0207822602	-0.02080699817014	0.1189
P_7	-0.0595969707	-0.05996367310289	0.6115
P_8	-0.0234767608	-0.02450930739531	4.2129
P_9	0	-0.00110319602355	100.0000
P_{10}	0	-0.00023846410765	100.0000
P_{11}	0.0173795968	0.01756346900581	1.0469
P_{12}	0	0.04962180835857	100.0000
P_{13}	0	0.00339941490416	100.0000
P_{14}	-0.0355144888	-0.10342461981940	65.6615
P_{15}	0	-0.00085846903721	100.0000
P_{16}	0	0.00893371292985	100.0000

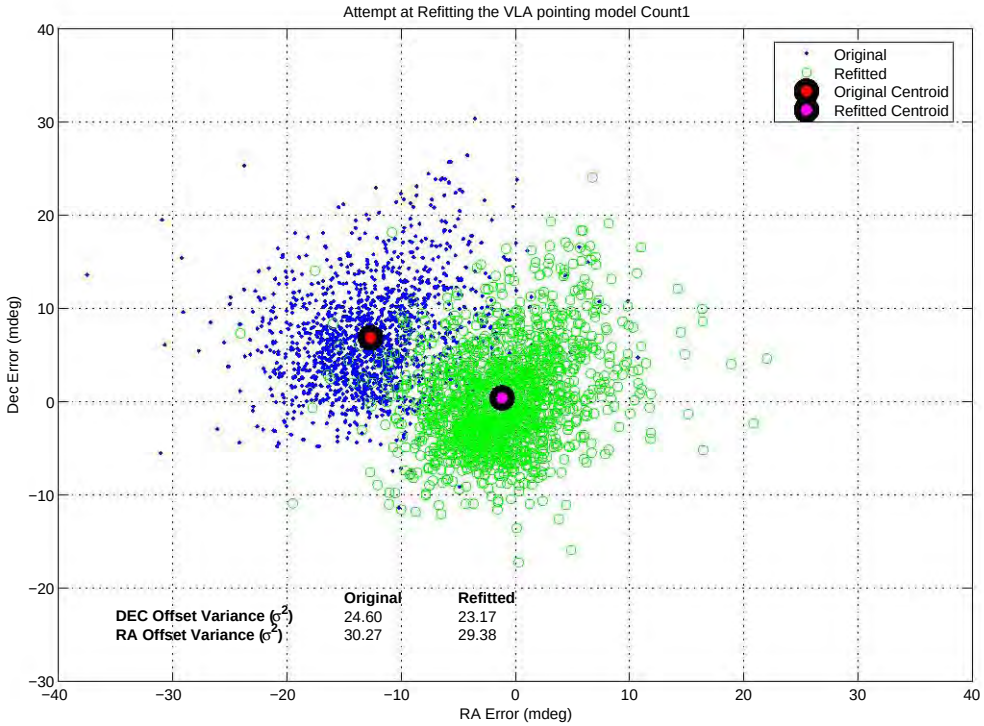

(a) Left Circularly Polarised Data

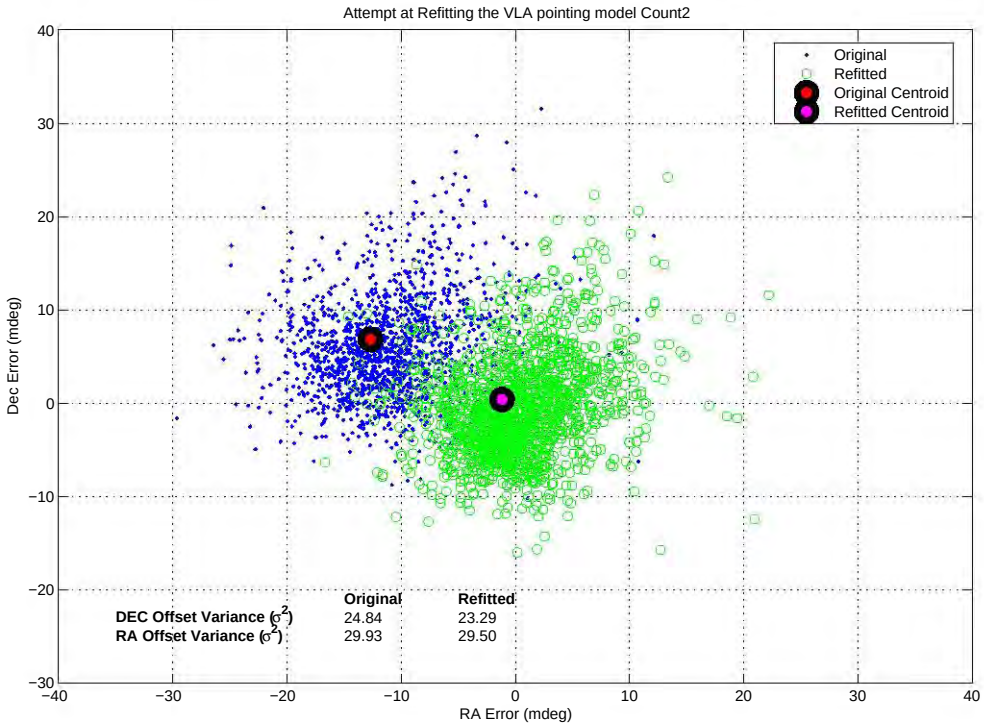

(b) Right Circularly Polarised Data

Figure 4.8: The effect of recalculating the parameters of the VLBI pointing model on the centroid of the observed pointing offset.

4.9 Summary

This chapter outlined the process of obtaining suitable measurements of pointing offsets starting with a description of the antenna and the way in which observations were performed.

Obtaining pointing measurements requires observations of a bright point source and in order to minimise gravitational effects on pointing, observations needed to be near to zenith. The pointing offset measurement was extracted from the observations by fitting an elliptical Gaussian to the data and using this to estimate the point of maximum signal. The typical uncertainty involved in fitting an elliptical Gaussian is negligible ($\ll$1 mdeg) compared to the 4 mdeg pointing requirement. For a point source, this position represents the observed position and, provided the point source position is known accurately, this can be used to obtain pointing offset measurements.

The data obtained from fitting the elliptical Gaussians was effected by at least 2, and possibly 3, pointing corrections applied by the HartRAO system. These include a refraction correction, the parameter based VLBI pointing model and Dr. Nicolson's original temperature model based on the day of year (which was only present for early data).

Dr. Nicolson's model needed to be removed where it had been applied, and after examining the resulting data, it was decided that it would be necessary to remove the VLBI pointing model effects, refit the parameters, and re-apply the updated VLBI pointing model to the data. This was to try to minimise data contamination from pointing effects accounted for under the VLBI pointing model. This had the effect of removing the systematic offset present in the pointing offset observations.

The data reduction (from observation to pointing measurement) was handled by a Fortran77 program. This processed data from the observation through to a pointing offset measurement, making all the required adjustments. The Fortran environment provided the necessary processing speed and produced a set of data files which included pointing offsets and temperatures.

Examination of these pointing offsets and modelling of the offsets based on temperature was subsequently handled by a set of MATLAB scripts. These scripts allowed the effectiveness of the different models to be examined in a high-level programming environment, with all the associated benefits that such an environment brings.

Chapter 5

Results

This chapter deals with the results of using the previously described modelling techniques to predict and thus remove pointing offsets. I begin by demonstrating that the pointing offsets obtained during this study are similar to those obtained by Dr. George Nicolson during a previous investigation. I then show conclusively that there is a relationship between the support temperatures and the pointing offset before describing the results of the different modelling techniques.

5.1 Comparison to the Existing Heuristic Model

As mentioned in Section 1.4, a previous study of the effect of temperatures on pointing offsets was carried out by Dr. George Nicolson. The results of a comparison between model and data are summarised in Figure 5.1a. Section 1.4 mentioned that substantial alterations were performed to the dish subsequent to Dr. Nicolson's study and that this may have effected to thermal pointing offsets. If the pointing offset is caused by changes in the support structure, it is likely that there will be a good agreement between the existing model and the data since the supports have not been altered. The original pointing correction model is shown in Figure 5.1a and the Declination and Right Ascension pointing offsets obtained during this study are shown in Figure 5.1b and Figure 5.1c respectively. Since Figure 5.1a shows the correction model, we would expect the observed pointing offsets to be a reflection of this correction model about the time axis. In Figure 5.1b and Figure 5.1c we see the Declination and Right Ascension pointing correction models mirrored by both the observed Declination pointing offset and the Right Ascension pointing offset. It appears that the two studies agree reasonably well.

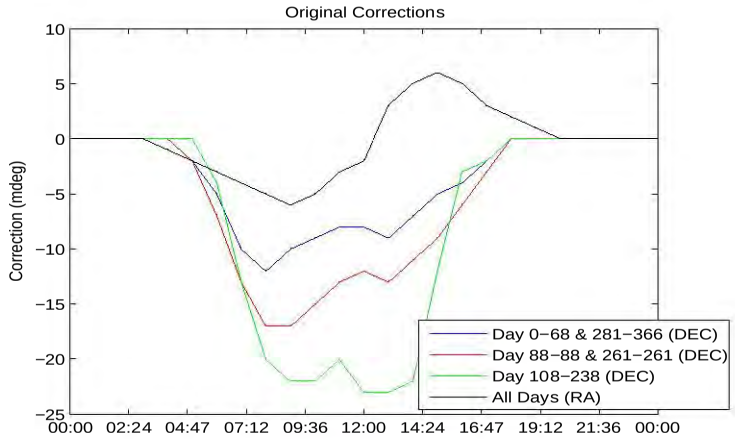

(a) The original pointing offset corrections derived by Dr George Nicolson.This is the pointing correction model which we expect to be a inverted relative to the pointing observations in Figures (b) and (c)

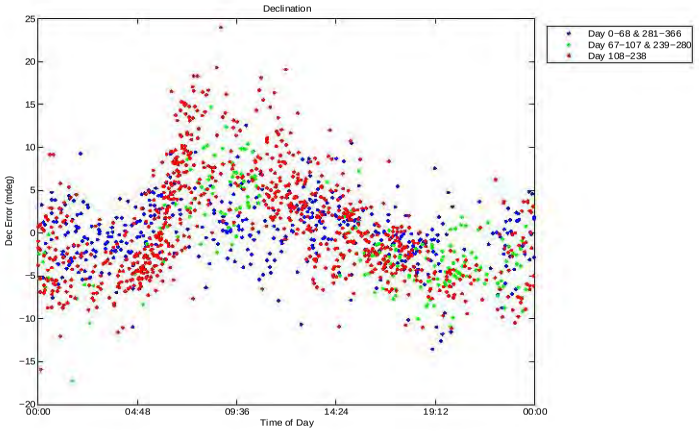

(b) The observed Declination pointing offsets wrapped into a 24 hour period. The observations are divided according to the day of year.

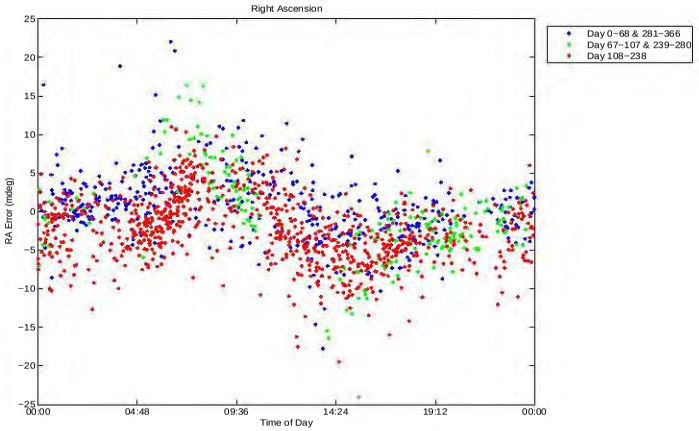

(c) The observed Right Ascension pointing offsets wrapped into a 24 hour period. The observations are divided according to the day of year.

Figure 5.1: A comparison of the original thermal pointing model and the pointing offsets obtained during these observations. Since we expect (a) to be the inverse of (b) and (c), we note that there is a general agreement between the previous study by Dr. Nicolson and the observations obtained during this investigation.

5.2 The Relationship Between Thermal Conditions and Pointing Offset

Two different techniques were used to demonstrate that there is a relationship between the support thermal conditions and the pointing offset.

The first was the use of correlation matrices. Correlation matrices are used as a means of seeing linear relationships between the different variables as described in Section 3.4. They were used to examine the relationship between various thermal properties of the supports and the Declination and Right Ascension pointing offsets.

The second method was to bin the pointing offsets according to different thermal properties and to see if the centroid of the binned pointing offsets moved as the thermal properties changed.

Both methods show that there is a relationship between the temperature difference across the Declination supports and the Declination pointing offset, however the Right Ascension pointing offset does not have a clear relationship to the recorded thermal conditions. This is demonstrated graphically in Subsection 5.2.3 when the Declination and Right Ascension pointing offsets are plotted against the temperature difference between Declination and Hour Angle supports respectively.

5.2.1 Correlation Matrix

Two correlation matrices were formed. The first correlation matrix used the antenna support temperatures, the ambient air temperature and the pointing offsets of the two axes. The second used the temperature differential between opposing suppports (i.e AT1-AT2, AT3-AT4 ... AT9-AT10) and the pointing offsets of the two axes. The correlation matrices are included in Table 5.1 and Table 5.2. Table 5.2 shows that there is a correlation between the temperature differential between Declination supports and the Declination pointing offset.

The highest correlation coefficients ($R_{ij} > 0.99$) highlighted in Table 5.1 show that there is a strong correlation between the North facing Declination supports (AT1, AT3, AT5 and AT7), and a strong correlation between the South facing Declination supports (AT2, AT4, AT6 and AT8). This is to be expected since there should be a strong relationship between thermistors with the same North-South orientation relative to the Sun.

The correlation coefficients between the Hour Angle support thermistor measurements are also high. This correlation is because the Hour Angle support thermistor temperatures shown in Figure 1.3 are not as strongly influenced by solar illumination since they are orientated East-West. A significant temperature differential between the Hour Angle supports does not develop. This is in contrast to the lower correlation coefficients between the North-South

oriented Declination thermistor temperatures (the temperatures are shown in Figure 1.2) which show a greater temperature differential developing due to the solar illumination effect.

It is interesting to note the high correlation coefficients between the South East Declination support thermistor readings (AT6 and AT8) and the Hour Angle support thermistor readings (AT9 and AT10). The correlation coefficients between the South West Declination supports thermistor readings are high ($R_{ij} > 0.98$), however this relationship is not as strong as the previously mentioned one. I have not been able to explain these correlations satisfactorily.

The correlation matrix shows a high degree of redundancy of the data. Later in this chapter Principle Component Analysis is used to reduce the dimension of the data, and examine the effectiveness of the new data as a possible input.

The second correlation matrix (Table 5.2) shows strong correlation between the Declination support temperature differentials and the Declination pointing offset, as expected from the simple linear model outlined in Section 3.3 and the investigation in Section 5.2.2. The strongest relationship is between AT5-AT6 and the Declination pointing offset, with a correlation coefficient of $R = 0.77350$. This shows that the temperature differential between the East facing Declination supports (AT5 is the top NE thermistor and AT6 is the top SE thermistor) is the most strongly correlated to the Declination pointing offset. The Declination angle encoder is mounted on the East side of the Declination axis, which may play a role in causing this observation. There is not a strong relationship between the Hour Angle support temperature differentials and the Right Ascension pointing offsets.

Table 5.1: Correlation Matrix (R) of the support temperatures, the ambient temperature and the pointing offsets. High correlations ($R_{ij} > 0.99$) are highlighted in red and the diagonal is highlighted in blue

	AT1	AT2	AT3	AT4	AT5	AT6	AT7	AT8	AT9	AT10	Tambient	RA Offset	DEC Offset
AT1	1.00000	0.97634	0.99890	0.97029	0.99197	0.98417	0.99169	0.98133	0.98081	0.98674	0.95697	0.00427	0.14489
AT2	0.97634	1.00000	0.97429	0.99847	0.95889	0.99271	0.95691	0.99417	0.98814	0.98468	0.88770	-0.07281	-0.01128
AT3	0.99890	0.97429	1.00000	0.96841	0.99446	0.98449	0.99426	0.98146	0.98019	0.98632	0.96013	0.01582	0.15460
AT4	0.97029	0.99847	0.96841	1.00000	0.95260	0.99194	0.95057	0.99416	0.98882	0.98347	0.87863	-0.07854	-0.03424
AT5	0.99197	0.95889	0.99446	0.95260	1.00000	0.97823	0.99946	0.97372	0.97096	0.98018	0.96787	0.06757	0.19581
AT6	0.98417	0.99271	0.98449	0.99194	0.97823	1.00000	0.97630	0.99937	0.99128	0.99194	0.91575	-0.00382	0.03467
AT7	0.99169	0.95691	0.99426	0.95057	0.99946	0.97630	1.00000	0.97180	0.96989	0.97897	0.96952	0.06743	0.20174
AT8	0.98133	0.99417	0.98146	0.99416	0.97372	0.99937	0.97180	1.00000	0.99104	0.99069	0.90838	-0.01385	0.01888
AT9	0.98081	0.98814	0.98019	0.98882	0.97096	0.99128	0.96989	0.99104	1.00000	0.99379	0.91996	-0.02935	0.04011
AT10	0.98674	0.98468	0.98632	0.98347	0.98018	0.99194	0.97897	0.99069	0.99379	1.00000	0.93626	0.01334	0.06968
Tambient	0.95697	0.88770	0.96013	0.87863	0.96787	0.91575	0.96952	0.90838	0.91996	0.93626	1.00000	0.12997	0.30499
RA Offset	0.00427	-0.07281	0.01582	-0.07854	0.06757	-0.00382	0.06743	-0.01385	-0.02935	0.01334	0.12997	1.00000	0.25268
DEC Offset	0.14489	-0.01128	0.15460	-0.03424	0.19581	0.03467	0.20174	0.01888	0.04011	0.06968	0.30499	0.25268	1.00000

Table 5.2: Correlation Matrix (R) of the temperature differential between axis supports and the pointing offsets. The highlights draw attention to the correlation between the Declination pointing offsets and the Declination support temperature differentials ($AT_i - AT_j$)

	AT1-AT2	AT3-AT4	AT5-AT6	AT7-AT8	AT9-AT10	RA Offset	DEC Offset
AT1-AT2	1.00000	0.95309	0.91820	0.92094	-0.38728	0.35479	0.71697
AT3-AT4	0.95309	1.00000	0.93573	0.94380	-0.40159	0.37480	0.72730
AT5-AT6	0.91820	0.93573	1.00000	0.98433	-0.36820	0.34244	0.77350
AT7-AT8	0.92094	0.94380	0.98433	1.00000	-0.35470	0.34125	0.76615
AT9-AT10	-0.38728	-0.40159	-0.36820	-0.35470	1.00000	-0.38297	-0.26539
RA Offset	0.35479	0.37480	0.34244	0.34125	-0.38297	1.00000	0.25268
DEC Offset	0.71697	0.72730	0.77350	0.76615	-0.26539	0.25268	1.00000

5.2.2 Binning of the Pointing Offsets

A binning procedure was used to confirm the dependence of pointing offset on temperature. The observations were grouped according to various classes of temperature (i.e ambient air temperature and both Declination and Hour Angle support temperature differentials), and the corresponding pointing offsets were plotted. The results are shown in Figure 5.2, 5.3 and 5.4. These show that the pointing offset does vary with the temperature difference between Declination supports (Figure 5.2) in agreement with Table 5.2, but does not vary significantly with the temperature differential between the Hour Angle supports (Figure 5.3) or the ambient air temperature (Figure 5.4).

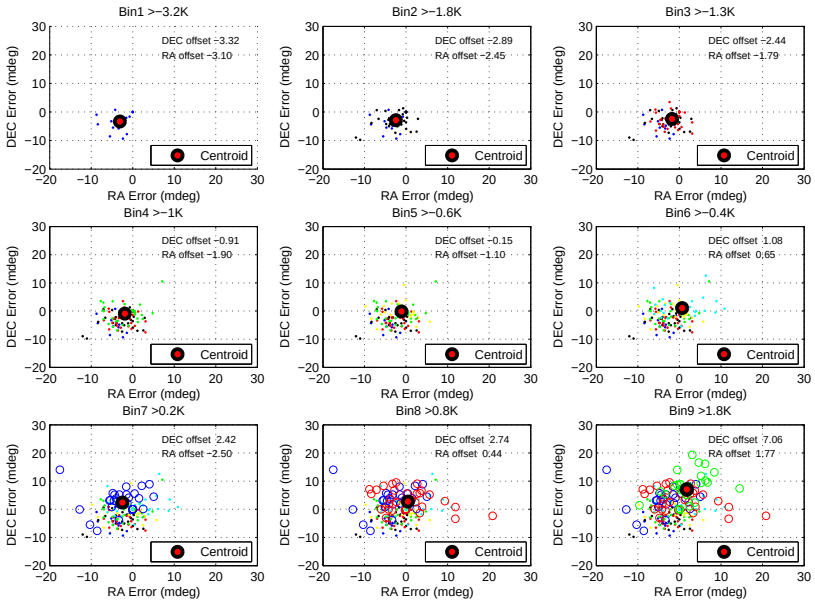

Figure 5.2: The pointing offsets are binned according to the temperature differential between AT5 and AT6 (see Table 1.1 for the locations of the thermistors). This is the temperature difference between Declination supports and can be written as AT5-AT6. We see the position of the pointing offset moving with bin number which implies a dependence of the pointing offset on AT5-AT6.

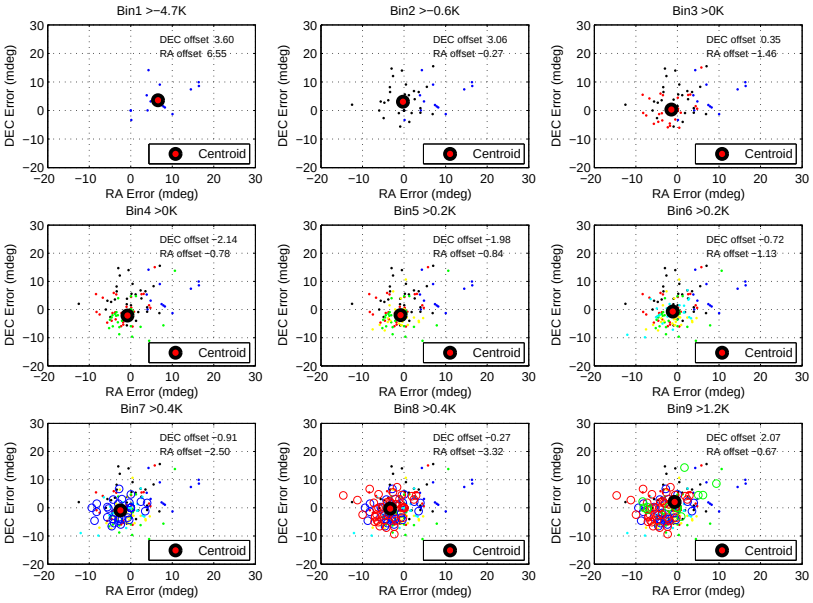

Figure 5.3: These graphs show the data binned using AT9-AT10 (see Table 1.1). This is the temperature difference between the Hour Angle supports. The graph does not show any marked relationship between the pointing offset and the temperature difference AT9-AT10. If there were we would see the pointing offset change with bin number.

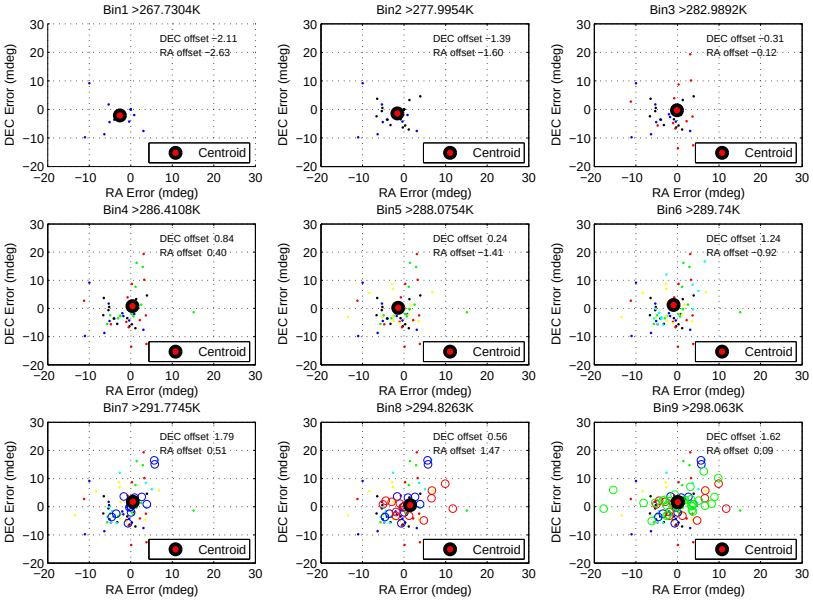

Figure 5.4: In this case the pointing offsets are binned according to the ambient temperature at the time of the observation. There is no clear dependence of the pointing offset on the ambient temperature. If this was the case we would be able to see the grouping of the pointing offset change with different bins.

5.2.3 Linear Fitting of the Pointing Offset to the Temperature Differential

The correlation matrix and the binning procedure outlined earlier both suggest a relationship between the Declination pointing offset and the temperature difference between the Declination supports. The data set that looked most promising was AT5-AT6 (see the correlation matrix in Table 5.2), and I pursued this as a starting point. The results are summarised in Figure 5.5a which show a strong relationship between the Declination support temperature differentials and the Declination pointing offsets.

This was not true for the Right Ascension pointing offsets which showed no correlation between pointing offset and Hour Angle (Right Ascension) support structure temperature differential (AT9 and AT10). These results are shown in Figure 5.5b.

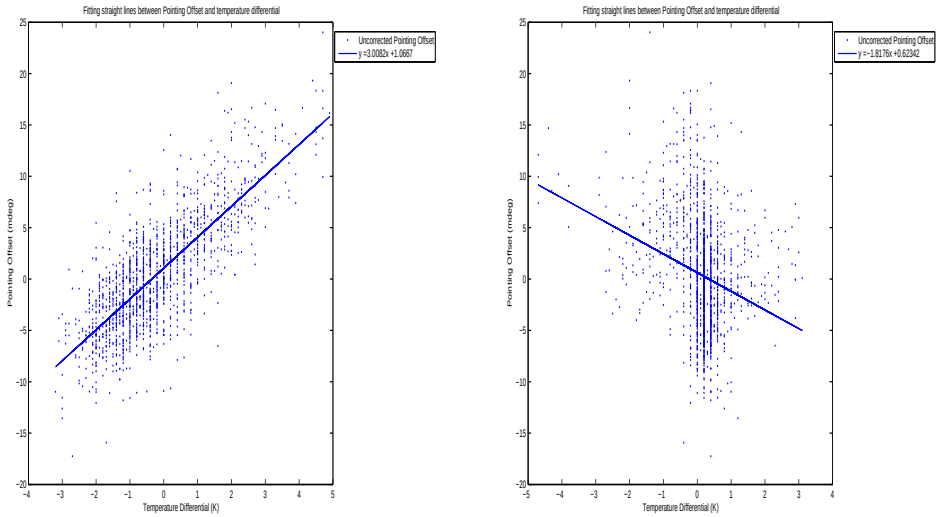

(a) The relationship between the Declination support temperature differential (AT5-AT6) and the Declination pointing offset.

(b) The relationship between the Hour Angle support temperature differential (AT9-AT10) and the Right Ascension pointing offset.

Figure 5.5: The relationships between the temperature differentials of various support struts and the pointing offset.

5.3 Simple Physical Model of the Declination Supports

A simple model of the Declination pointing offsets is described in Section 3.3 and assumes that Declination pointing offsets are caused entirely by deformations of these Declination supports. While this is unlikely to provide a comprehensive result, it is interesting to see how successful the model is. To investigate this I plotted the actual Declination offsets against those predicted by the model with the results shown in Figure 5.6. The results were promising and gave credibility to the theory that the Declination pointing offsets were caused by thermal expansion and deformation of the Declination supports. The data used has the VLBI pointing

model parameters refitted as described in Section 4.8.

Refining the approximations of this model further may produce better results, however such improvements are limited by the costs involved (as already discussed with reference to FEA). Thus the results are left at this stage as a further piece of evidence that the Declination support temperatures play a part in causing the Declination pointing offset, and that this is a reasonable foundation from which to begin investigating.

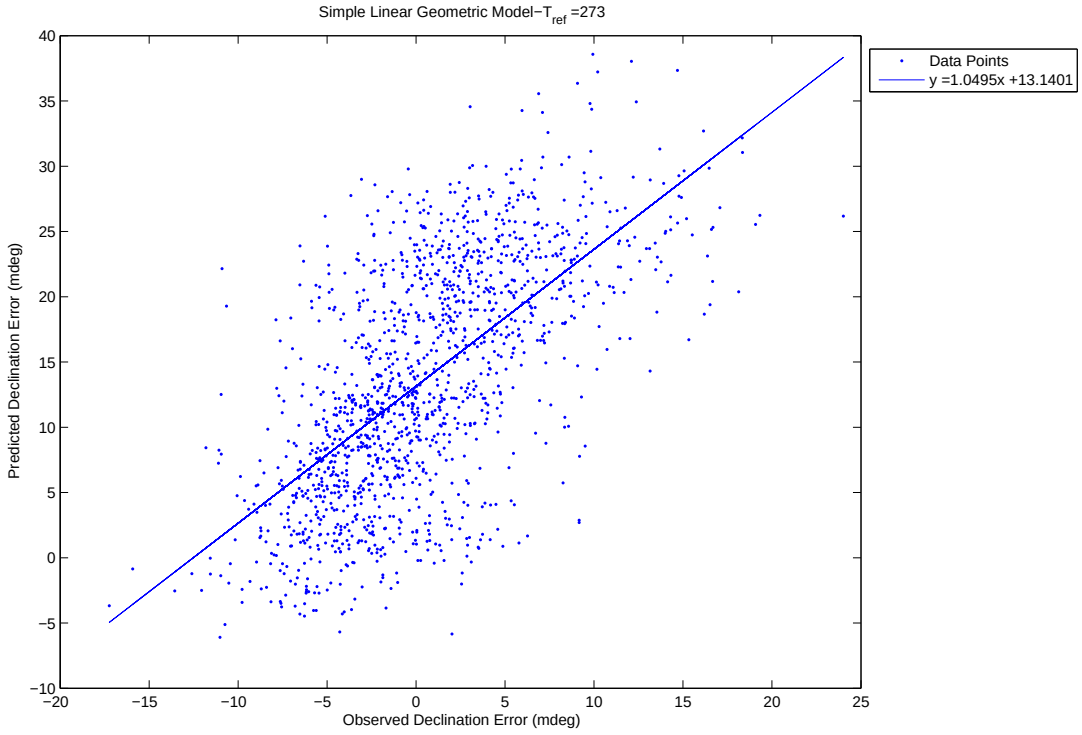

Figure 5.6: The correlation between the Declination pointing offset predicted by a simple geometric model (described in Section 3.3) of the telescope and the actual observed offsets.

5.4 Principle Component Analysis

As explained earlier Principle Component Analysis (PCA) seeks to redefine a data set in terms of a new basis, so as to maximise the Signal-to-Noise ratio and to minimise data redundancy. The effect is that the vectors formed from the new basis are both orthonormal to each other and ordered in terms of decreasing variance so that the first Principle Component has a greater variance than the second Principle Component and so forth.

Since each of the Principle Components is orthonormal and linearly independent (as they form a basis of the vector space), it is interesting to see if there is any correlation between the Principle Components and the pointing offsets. Correlation matrices are included in

Table 5.3 and Table 5.4, and the first three Principle Components are shown in Figure 5.7 and Figure 5.8. The Principle Components used in Table 5.3 and Figure 5.7 are derived from all the thermistor readings while the Principle Components used in Table 5.4 and Figure 5.8 use only the Hour Angle thermistors.

Table 5.3 shows that there is a good correlation between the second Principle Component and the Declination offset (R=0.7657), but that there is no such correlation between any of the Principle Components and the Hour Angle offset. I have included Table 5.4 to demonstrate that the Hour Angle thermistor readings are definitely not linearly related to either of the pointing offsets. Table 5.4 does not show any correlation between Principle Components of the Hour Angle thermistors and the Hour Angle pointing offset.

In terms of the temperature data, the first Principle Component (i.e the vector with the greatest variance) will represent the large scale, diurnal temperature variation experienced by the thermistors, which we expect to have the largest variation. The second Principle Component will represent the next smallest variation of the data, which is likely to be the difference between the individual temperatures and the large scale diurnal temperature variations. If this is true then the second Principle Component is likely to be related to temperature difference between supports. This relationship is shown in Figure 5.9, which shows the clear linear relationship between the Declination support temperature differential, AT5-AT6, and the second Principle Component. Figure 5.10a shows that there is a strong linear relationship between the second Principle Component and the Declination offset as is expected from the large correlation between these two indicated by Table 5.3

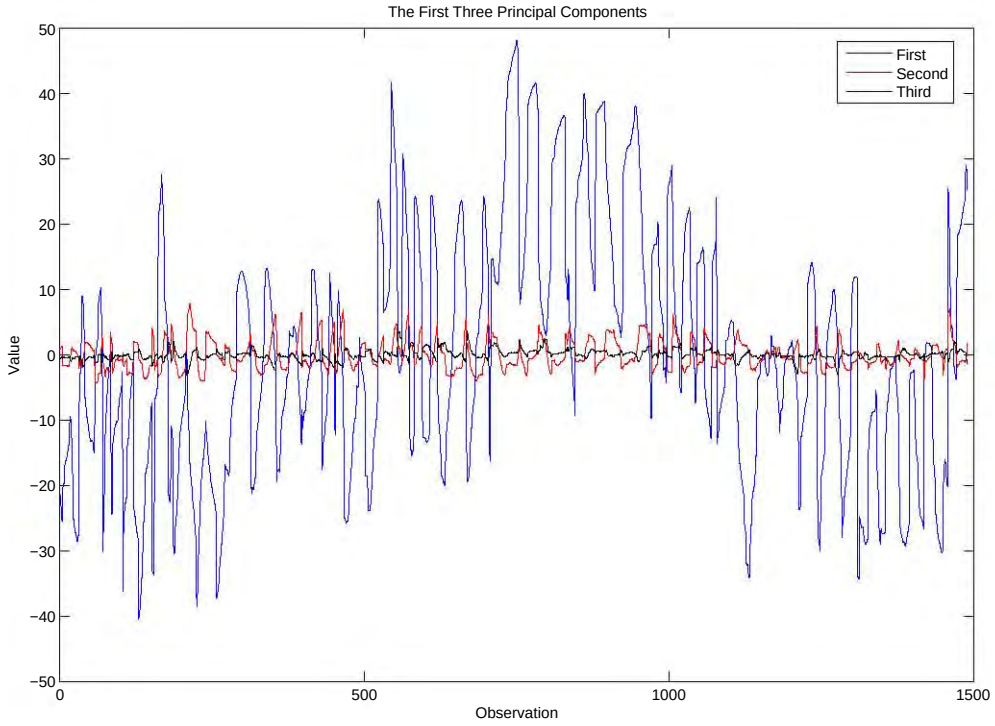

Figure 5.7: The Principle Components of the Declination Support temperatures

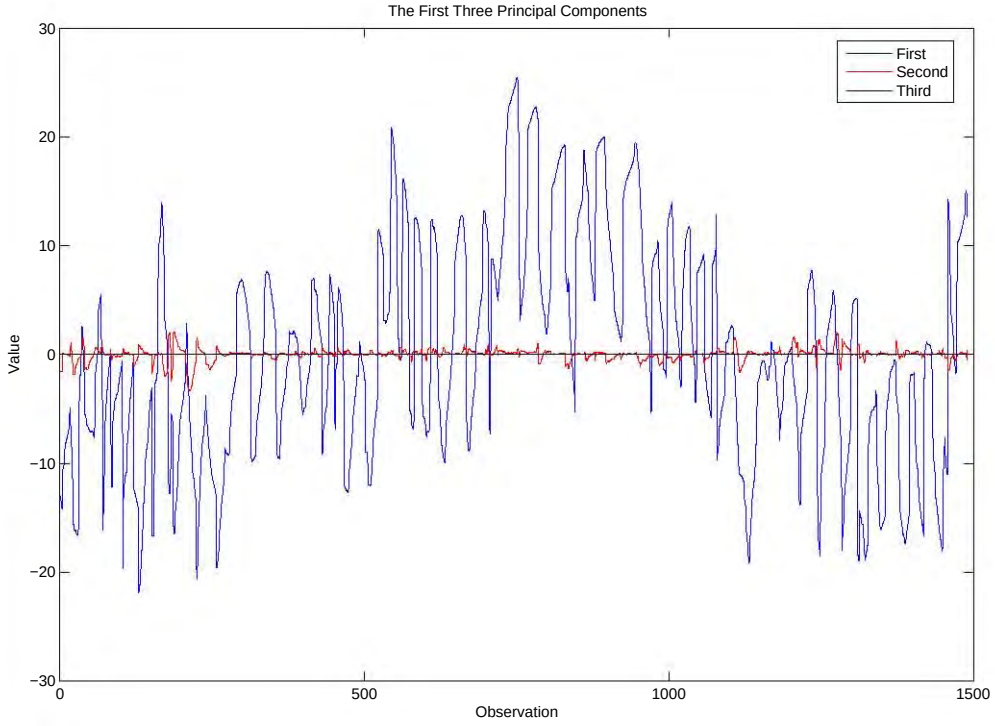

Figure 5.8: The Principle Components of the Hour Angle Support temperatures

Table 5.3: Correlation matrix between the Principle Components of all thermistor readings and the pointing offsets.

PC	1	2	3	4	5	6	7	8	9	10	RA Offset	DEC Offset
1	1.00000	0.00000	0.00000	0.00000	-0.00000	0.00000	-0.00000	-0.00000	0.00000	-0.00000	0.01148	-0.07010
2	0.00000	1.00000	0.00000	-0.00000	-0.00000	-0.00000	-0.00000	0.00000	-0.00000	0.00000	0.40332	0.76757
3	0.00000	0.00000	1.00000	0.00000	-0.00000	0.00000	-0.00000	-0.00000	0.00000	-0.00000	-0.19638	-0.03062
4	0.00000	-0.00000	0.00000	1.00000	0.00000	-0.00000	0.00000	0.00000	-0.00000	-0.00000	0.41210	-0.06287
5	-0.00000	-0.00000	-0.00000	0.00000	1.00000	0.00000	-0.00000	-0.00000	-0.00000	-0.00000	0.17813	-0.07955
6	0.00000	-0.00000	0.00000	-0.00000	0.00000	1.00000	0.00000	-0.00000	-0.00000	-0.00000	-0.09622	0.09810
7	-0.00000	-0.00000	-0.00000	0.00000	-0.00000	0.00000	1.00000	0.00000	0.00000	0.00000	-0.04416	-0.00890
8	-0.00000	0.00000	-0.00000	0.00000	-0.00000	-0.00000	0.00000	1.00000	-0.00000	-0.00000	-0.03963	-0.06084
9	0.00000	-0.00000	0.00000	-0.00000	-0.00000	-0.00000	0.00000	-0.00000	1.00000	0.00000	-0.04563	-0.01736
10	-0.00000	0.00000	-0.00000	-0.00000	-0.00000	-0.00000	0.00000	-0.00000	0.00000	1.00000	0.02047	0.05204
RA Offset	0.01148	0.40332	-0.19638	0.41210	0.17813	-0.09622	-0.04416	-0.03963	-0.04563	0.02047	1.00000	0.25268
DEC Offset	-0.07010	0.76757	-0.03062	-0.06287	-0.07955	0.09810	-0.00890	-0.06084	-0.01736	0.05204	0.25268	1.00000

Table 5.4: Correlation matrix between the Principle Components of only the Hour Angle thermistor readings and the pointing offsets.

PC	1	2	RA Offset	DEC Offset
1	1.00000	-0.00000	0.01577	-0.04441
2	-0.00000	1.00000	-0.38411	-0.27573
RA Offset	0.01577	-0.38411	1.00000	0.25268
DEC Offset	-0.04441	-0.27573	0.25268	1.00000

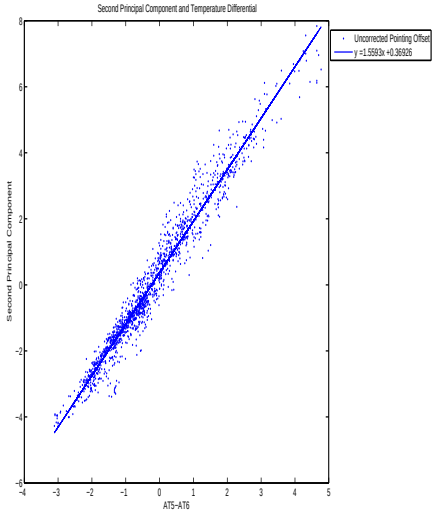

Figure 5.9: The second Principle Component plotted against the Declination temperature differential, AT5-AT6

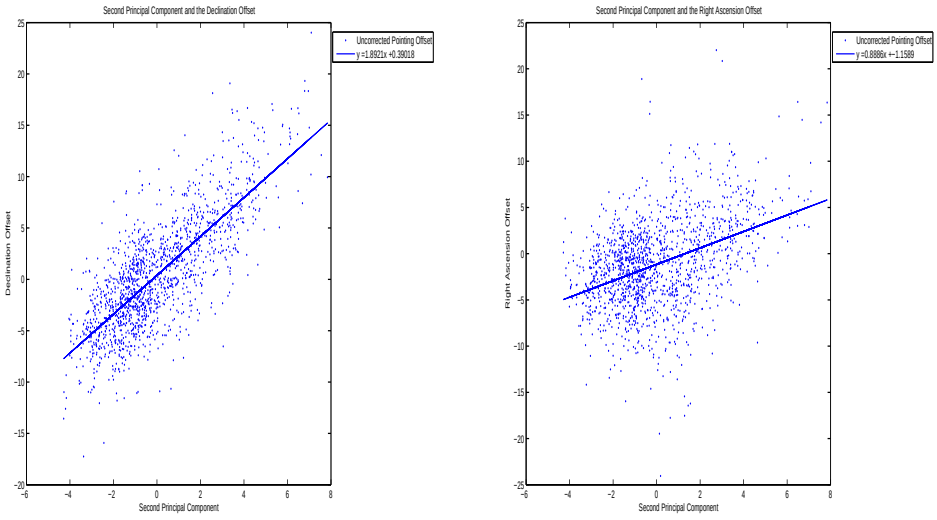

(a) The relationship between the second Principle Component and the Declination pointing offset

(b) The relationship between the second Principle Component and the Right Ascension pointing offset

Figure 5.10: Pointing offsets and the second Principle Component

5.5 Linear Fitting of a Weighted Combination

The technique of using weighted inputs was introduced in Equation 3.11, Section 3.11. Equation 3.11 is repeated here for clarity

$$\text{Model Pointing Offset} = \sum_{i=1}^{i=n} a_i AT_i \tag{5.1}$$

The technique involves weighting the n inputs, AT_i, with the coefficients a_i, and varying the weights until the difference between the model pointing offset and the observed pointing offset is minimised. Larger weighting coefficients correspond to a better linear relationship between the input and the pointing offset.

5.5.1 Weighted Temperatures

Based on the relative success of the simple linear model and the clear relationship between the temperature differential and the Declination pointing offset, it seemed sensible to try and fit a model using the individual temperature readings as inputs, AT_i, to the model in Equation 5.1. It is important to note that this model is potentially compromised by the large redundancy between the variables (shown in Table 5.1). The fitting procedure may not work properly due to this redundancy, however the results are still interesting.

Since this model requires fitting to data, it is important to separate the data into a training set and a testing set. I removed 100 randomly selected data points from the fitting and used these as test points. The model was fitted on the remaining data points and the result of this model when applied to the test data points is shown in Figure 5.11.

One of the things that becomes apparent from Figure 5.11d, is the marked effect that AT5 and AT6 have on fitting to the Declination pointing offset. These are the thermistors located at the top of the the North-East and South-East Declination supports. The angle encoders are located on the East of the Declination supports and this may be why thermal deformations of these supports appear to be significant in causing Declination pointing offsets. This agrees with Section 5.2.1, which finds that the greatest correlation is between the temperature differential between AT5 and AT6 and the Declination pointing offset (R=0.7735).

This model shows a marked improvement for the Declination pointing offset (45%), however the Right Ascension pointing offset only improves by 27%. This might be improved by increasing the number of thermistors along the Hour Angle supports.

5.5.2 Weighted Principle Components

As noted earlier, a large fraction of the temperature data is redundant. Redundant data is often problematic when fitting, due to the presence of a large number and extent of local minimums. Since the Principle Components minimise the redundancy, it seems sensible to attempt the same procedure outlined in the subsection 5.5.1, but using the Principle Components as the inputs AT_i. We expect the largest weighting (and hence best linear correlation) for the Declination pointing model to correspond to the second Principle Component since the highest correlation coefficient between the Principle Components and the Declination pointing offset occurs with the second Principle Component (see Table 5.3). The same correlation matrix suggests that the Right Ascension model will perform poorly (since there are no large correlation coefficients between the Right Ascension pointing offsets and the Principle Components). The results are shown in Figure 5.12. Figure 5.12d shows that the largest positive weighting for the Declination pointing offset model is given to the second Principle Component as expected.

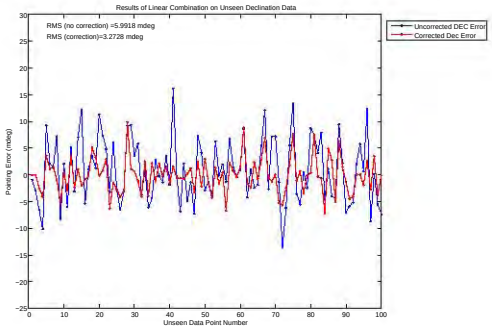

(a) Result of weighting of temperatures to model and correct the Declination pointing offset

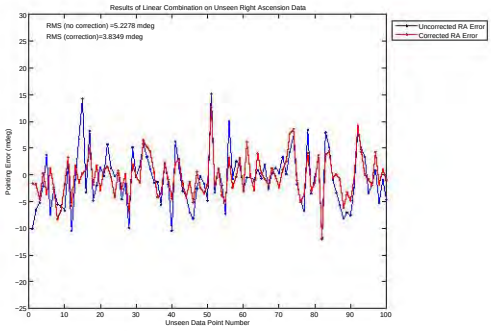

(b) Result of weighting of temperatures to model and correct the Right Ascension pointing offset

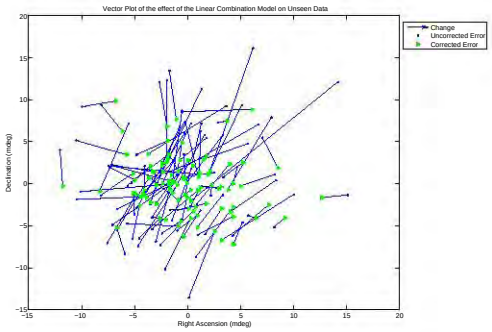

(c) Results of weighting of temperatures to model and correct the pointing offsets on both axes. This shows (a) and (b) on the same graph for clarity.

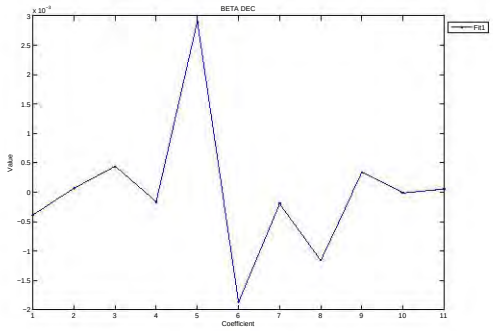

(d) Declination Model. The weightings accorded to the thermistor temperatures when fitting to the Declination pointing offset

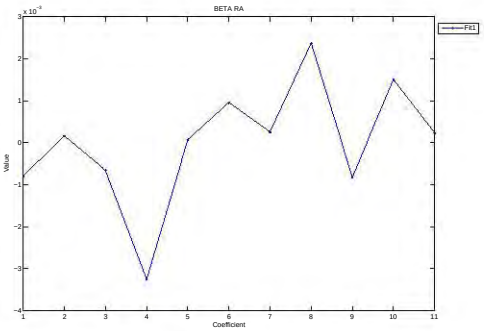

(e) Right Ascension Model. The weighting accorded to the thermistor temperatures when fitting to the Right Ascension pointing offset.

Figure 5.11: Weighted linear combination of the temperatures using AT1 → AT10 and $T_{ambient}$ (represented by coefficient 11).

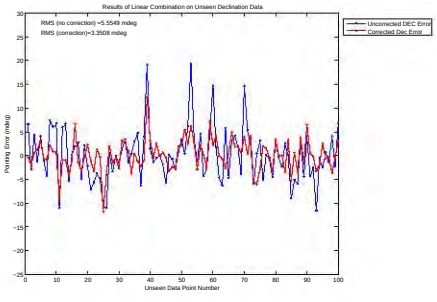

(a) Result of weighting the Principle Components to model and correct the Declination pointing offset

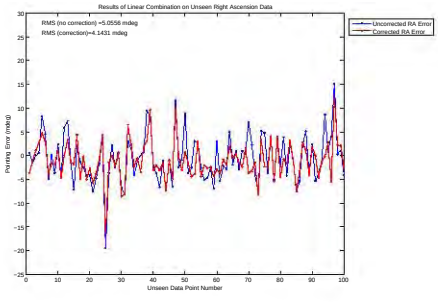

(b) Result of weighting the Principle Components to model and correct the Declination pointing offset

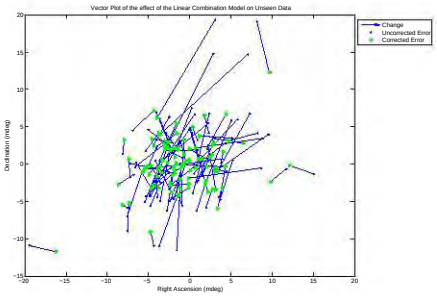

(c) Pointing offset improvement using weighted Principle Components for both axes

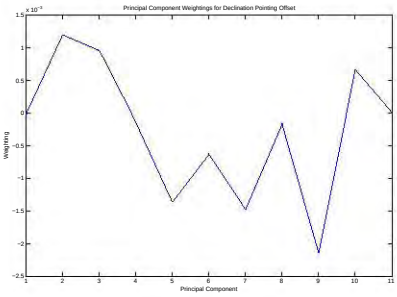

(d) Weightings assigned to the Principle Components for the Declination pointing offset

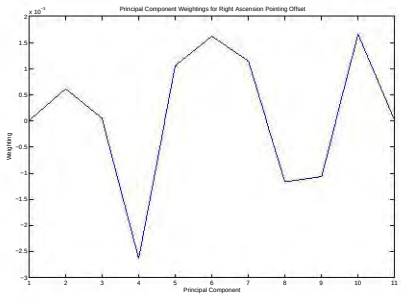

(e) Weightings assigned to the Principle Components for the Right Ascension pointing offset

Figure 5.12: Weighting the Principle Components as a means of modelling the pointing offsets

5.6 Using the VLBI Pointing Model and Temperature Binning as a Solution

One way of trying to understand any temperature induced twisting effects would be to use the VLBI Pointing Model[1] as a physical model, and fitting this function to data binned according to a temperature criteria. It would be necessary to identify which of the parameters in the VLBI model might be susceptible to temperature variations, and to allow these to vary while keeping the others fixed. We would then be able to roughly determine how the fitted coefficients varied as a function of temperature.

This is potentially useful. Certain VLBI coefficients are related to twisting effects of the axes. This may occur due to temperature variations and, if this was the case, it would be revealed by any variations of the parameters with temperature. Descriptions of the coefficients which may be effected by temperature variations are shown in Table 5.5, with the full list included in Appendix B.

The effects on the coefficients once fitted to binned data are shown in Figure 5.13a. Little physical information is revealed by the process (indeed it seems to say that the Perpendicular Axis Skew and the "Tilt Over" effects mirror one another), however using the different coefficients as corrections for the various bins does appear to be effective when the corrected pointing offsets shown in Figure 5.14 are compared to the uncorrected pointing offsets shown in Figure 5.2. The pointing offsets remain roughly constant (compared to the variation seen in Figure 5.2) in each bin once the varying VLBI models are applied to each bin.

What is particularly interesting in 5.13a is that Coefficient 3 and Coefficient 6 mirror each others behaviour. It is difficult to gain any real physical information about what is happening from these graphs apart from the observation that the effect (P_5) appears to vary in an almost sinusoidal manner as the Declination temperature differential increases.

Table 5.5: Description of the fitted VLBI Pointing Model Coefficients (Himwich, 1993)

Coefficient	Description
P_3	Perpendicular Axis Skew
P_5	"Tilt Out"
P_6	"Tilt Over"

The results for the Declination pointing offsets are fairly good and can be seen in Figure 5.13c. These show the RMS of the pointing offset both before and after the correction has been applied. The Right Ascension pointing offset does not vary with the temperature differential between the Hour Angle supports suggesting that a different method will need to be employed to obtain a model for the Right Ascension pointing offsets.

[1] see Appendix B for further information on the VLBI pointing model and coefficients

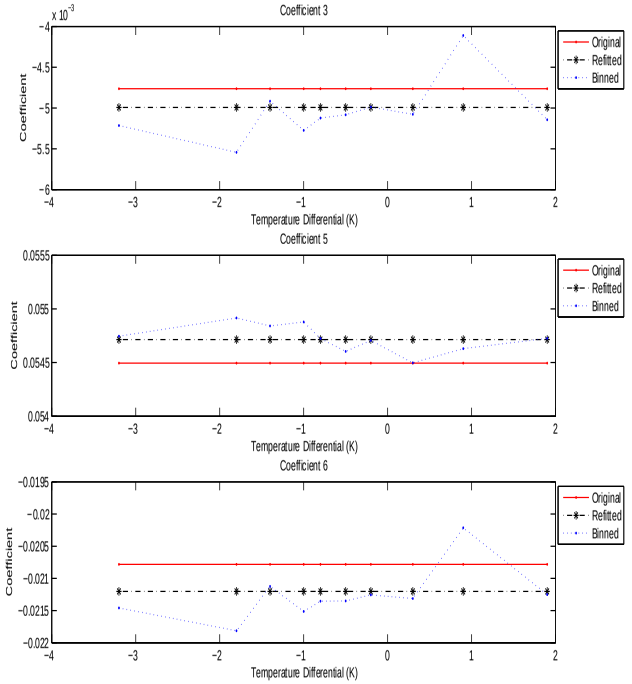

(a) Fitting the VLBI model to data binned according to the AT5-AT6 temperature differential. We can clearly see how the parameters vary with temperature differential.

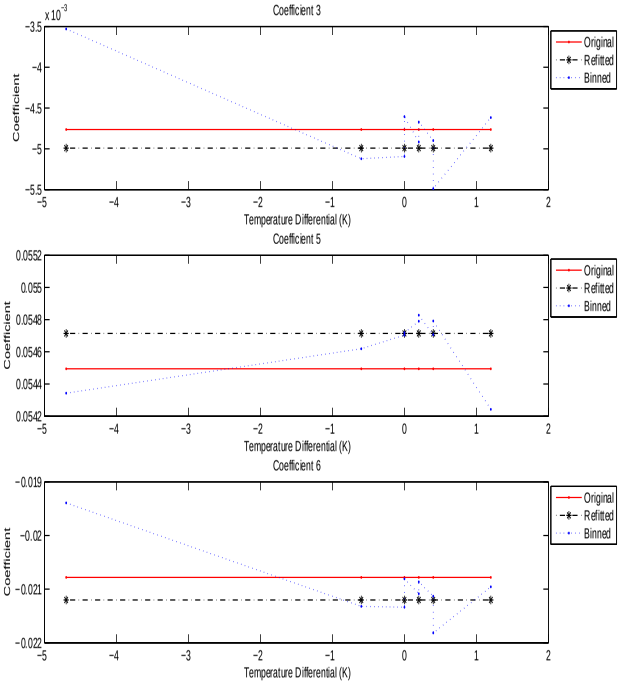

(b) Fitting the VLBI model to data binned according to the AT9-AT10 temperature differential.

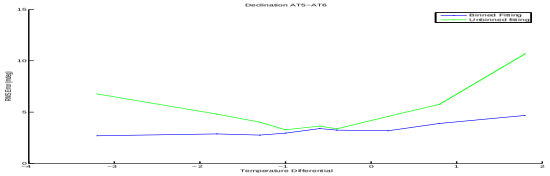

(c) The effects on the RMS of the pointing offsets using temperature binned according to the AT5-AT6 temperature differential for the Declination pointing offset

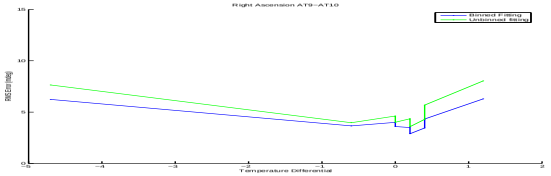

(d) The effects on the RMS of the pointing offsets using temperature binned according to the AT9-AT10 temperature differential for the Right Ascension pointing offset

Figure 5.13: The effect of fitting the VLBI coefficients to data binned according to thermal properties.

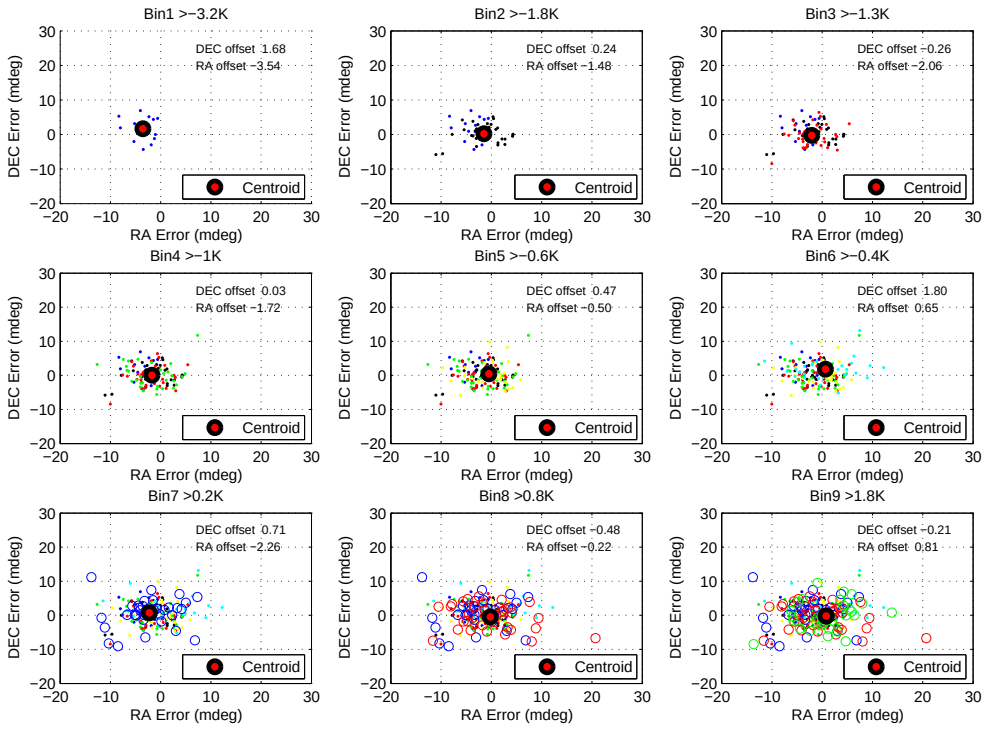

Figure 5.14: Graphs showing the corrected pointing offsets for each bin of the temperature differential AT5-AT6 as well as the mean Declination and Right Ascension pointing offset for each bin.

5.7 Neural Network

Neural networks present an interesting and promising solution to the problem. Neural networks are particularly useful in models where the underlying physical nature of the problem is not well understood. To demonstrate that a neural network is a feasible means of correcting the pointing offset, I set up a basic Neural Network and trained it using randomly selected data points.

5.7.1 Temperature Inputs

I chose to use the commonly utilised feed-forward back propagation network. I initially chose to have two layers of neurons. The first layer was comprised of 5 neurons and used a *tansig* transfer function (see Figure 3.2). The second layer was made of 2 neurons and used the *purelin* transfer function. The propagation algorithm used was the *Levenberg-Marquardt*. In order to avoid overfitting I used the *Early Stopping* technique and subdivided so that 25% was included in the validation data set, 25% was included in the test set, and the remaining 50% was used for training data.

I preprocessed the data by normalising the mean and standard deviation of the data using MATLAB's *prestd()* function. This is a standard step in training neural networks and allows for more efficient training. I used Principle Component analysis to discard any data that contributed less than 1% of the variance. This left me with only the first and second Principle Components, which contained over 99% of the data variation. The results of applying the model correction to unseen data are shown in Figure 5.15. The results were promising, particularly with regards to correcting the Declination pointing offset.

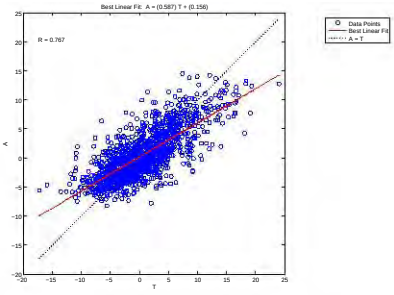

(a) A regression analysis of the predicted Declination offset against the observed offset.

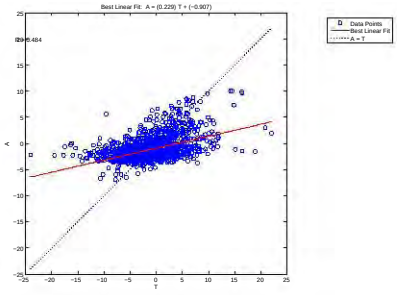

(b) A regression analysis of the predicted Right Ascension offset against the observed offset.

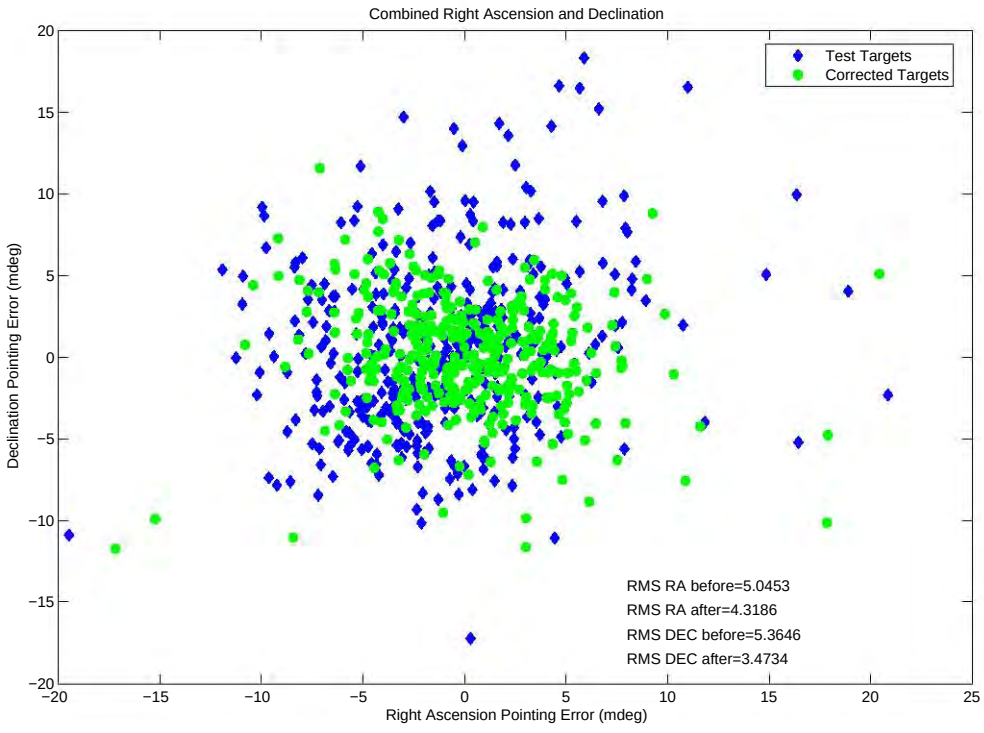

(c)

Figure 5.15: The results obtained using a neural network model trained on AT1→AT10 and $T_{ambient}$.

5.7.2 Neural Networks as a Substitute for the VLBI Pointing Model

Since the binning of the data and then refitting VLBI parameters had proved to be successful I decided to try to expand the Neural Network inputs to include the variables used in the VLBI fitting i.e Hour Angle and Declination as well as the support temperatures. I hoped that this would result in a trained neural network that could replace the VLBI pointing model and include thermal corrections as well. Typical results of this investigation are shown by Figure 5.16. I believe these to be a success. Figure 5.16 shows that a neural network could possibly be used as a pointing model to take all possible pointing offset contributions into account such as gravitational deformation, axis misalignments and more. The Right Ascension pointing offsets still appear to be problematic, however there is a clear improvement in general.

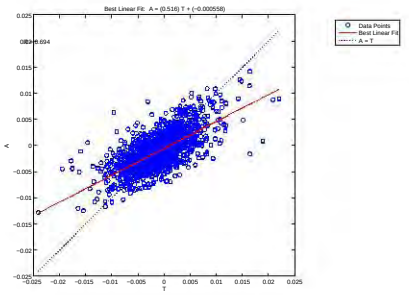

(a) Regression showing the predicted Right Ascension offset against the observed offset.

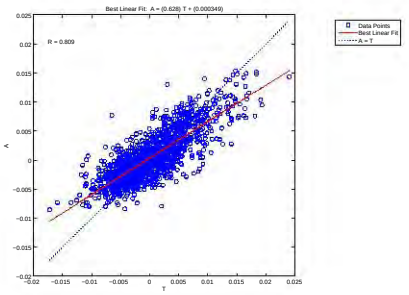

(b) Regression showing the predicted Declination offset against the observed offset.

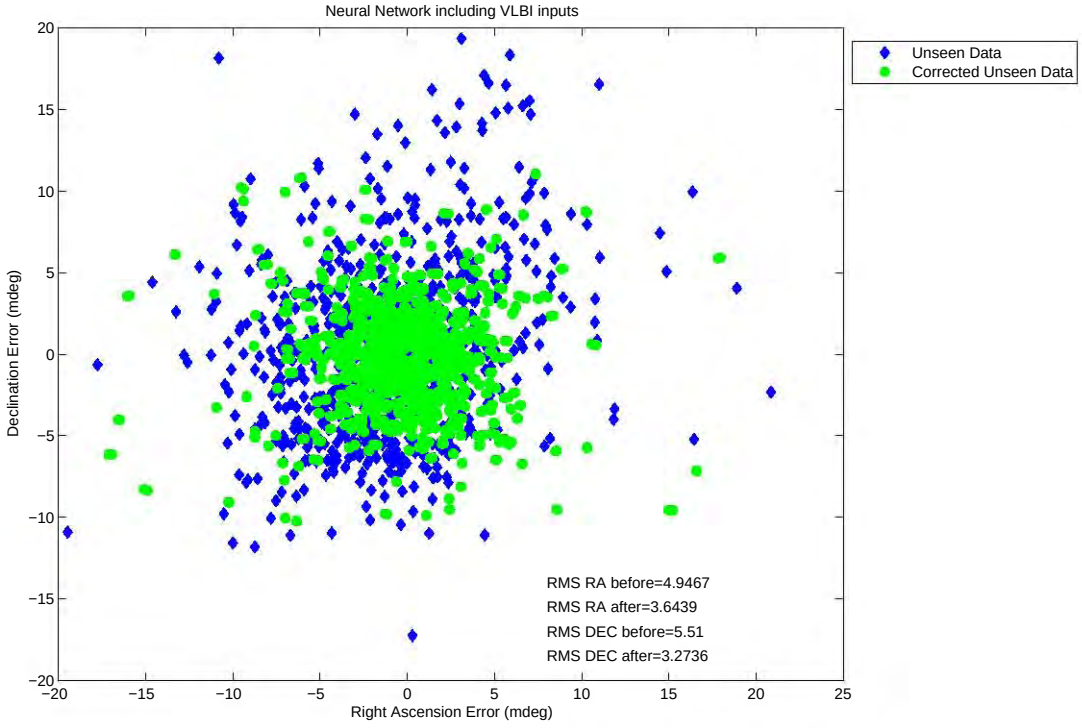

(c) The result of the neural network that incorporates VLBI inputs.

Figure 5.16: Neural network trained to replace the VLBI pointing model

5.8 Conclusions

This chapter has presented the results of a number of different approaches to modelling the pointing offset. It began by clarifying the relationship between the Declination support temperature differential and the Declination pointing offset, by using both a binning technique and a plot of the Declination support temperature differential againt the Declination pointing offset. A much weaker (perhaps even non-existent) correlation between Hour Angle support temperature differential and Right Ascension pointing offset is also apparent from this preliminary analysis. Principal Component Analysis shows a strong correlation between the Declination support temperature differential and the second Principal Component of the antenna support temperature, suggesting that this second Principal Component is a measure of the temperature difference between the Declination supports.

The relationship between Declination support temperature differential and the Declination pointing offset was then exploited by using the linear weighting of the temperature support temperatures and using a least squares fitting between the temperature of the supports and the Declination pointing offsets. This was also done for the Right Ascension pointing offset. The result of applying this model to the observations was a decrease in average Declination pointing offset from approximately 5.5 mdeg to approximately 3.2 mdeg (50% improvement). A much less convincing improvement of approximately 20% was achieved on the Right Ascension pointing offset.

A similar weighting scheme was then assigned to the Principal Components. This reflected the correlation between the Declination pointing offset and the second Principal Component which (after fitting) was assigned the most positive weighting.

Investigation proceeded by using the VLBI pointing model (and the twisting effects that it models) as a means of physically modelling the effects present on the telescope. If such twisting effects depend on thermal inputs, then it is likely that the VLBI parameters (which model twisting effects) will vary if the data is binned according to thermal inputs and the VLBI parameters are then fitted using data from each bin. This method had fairly good results, however it is prone to overfitting since the data sets in each bin are small.

A neural network model was then investigated using the temperatures as inputs and both the Declination and Right Ascension pointing offsets as targets. This had a similar level of success as the linear weighting model, producing improvements of the Declination offset of approximately 50% with poor results achieved on the Right Ascension pointing offset.

A final study showed that it may be possible to replace the VLBI parameter based model with a neural network which would have the Declination, Hour Angle and temperatures as

inputs and would produce a pointing correction. This would result in a single pointing correction model taking all pointing effects into account. It would also, however, mean that there would be less physical understanding of the pointing offset and that any major alterations to the antenna would probably require the model to be retrained.

Chapter 6

Conclusion

6.1 Different Modelling Methods

The results shown in the previous chapter are positive, particularly with respect to modelling the Declination pointing offsets. It appears that achieving an RMS pointing offset of less than 5 mdeg for both axes is realistically obtainable in the short term.

Using the VLBI model and fitting it to thermally binned data appears to give good results as shown in Figure 5.14. I have reservations about how successful a general application of this model would be as it has the additional problem of requiring a large number of observation to train successfully due to the dilutive effect binning the data.

Both the linear weighting and the neural network model give considerable (50%) improvement in the Declination pointing offset, however the Right Ascension pointing offset improvements are much less impressive (20%). The advantage of the linear weighting over the neural network is that the model is based on real underlying physical aspects, while the neural network needs to be carefully checked to ensure the predictions are not an anomaly of the training process.

As such I would recommend proceeding with the linear weighting method in the short term. It would be possible to have a neural network training in the background and tests could be done on the predictions of the neural network over time until reliable results can be expected with certainty. If the decision was made to switch to the neural network model sometime in the future, the linear weighting model could be maintained in the case of extensive dish modifications which may require retraining the neural network.

6.2 Possible Improvements

Further investigation should be carried out to determine the underlying physical cause of the Right Ascension pointing offsets, since none of the models implemented provides a completely satisfactory model for this axis. A suggestion from Prof. Heinz Ruther (U.C.T Geomatics

Department) would be to try and obtain laser scan point clouds of the structure at different times during the day during the winter period. These scans could highlight directly where deformations are occurring. With this knowledge it might be possible to derive a simple model to accurately account for the Right Ascension pointing offsets.

Alternatively a finite element model could be constructed from the laser scan dimensions and this could be used. Worth considering is that the backing structure of the telescope may be deforming as appears to happen at the Leighton Array at OVRO (Lamb and Woody, 2002) described in Section 2.3. Compensating for this would require installing a large number of temperature sensors across the backing structure and studying temperature differentials between these sensors.

Our understanding of the structural temperatures could be improved by using more temperature sensors across the structure. The results of this thesis indicate a relationship between pointing offset and Declination support temperatures. This suggests the need for more temperature sensors on the Declination supports for more comprehensive information. It would also be useful to place temperature sensors on any other Hour Angle supports to allow further insight to be gained on the possible causes of the Right Ascension pointing offset. Laser scans would be useful as a means of identifying critical points on the structure.

It would be useful to obtain more data, particularly over the 07h00→15h00 period when the pointing offset is most pronounced on the Declination axis. This would allow the model to be refined further and to produce better results in the future.

6.3 *Meer*KAT

These findings give an idea of the type of thermal deformations that may effect *Meer*KAT. Since these dishes will have different backing and support structures a great deal of this investigation is not entirely applicable, however this does show that simple models might be suitable for use on *Meer*KAT.

A great advantage with regards to *Meer*KAT would be the availability of structural drawings. These would allow FEA to be implemented very easily. A system of temperature sensors on the backing and support structure would allow real-time monitoring and correction of the thermal pointing offsets. Other loading effects such as wind could easily be incorporated into the model.

In order to take advantage of these options the new telescopes should be equipped with temperature sensors from the beginning. Areas of concern should be the backing structure and the primary axis supports, which require a larger temperature sensor density. The design may create other areas which are susceptible to thermal deformations. These would also

require careful temperature monitoring.

Bibliography

CBASS: C-Band All-Sky Survey, http://www.astro.caltech.edu/cbass/

Microchip, ENC28J60 Rev.B4 Silicon Errata-Datasheet

Mounting Instructions: ROC 415,416,417-Datasheet, Tranreut, Germany

NEC, RFT Training Manual, 1998

Microchip, ENC28J60-Datasheet, 2004

Analog Devices, Low Cost Precision IC Temperature Transducer-AD592*-Datasheet, Norwood, MA

Analog Devices, Microprocessor-Compatible 12-Bit D/A Converter-AD667*-Datasheet, Norwood, MA

Anderson, E., Bai, Z., Bischof, C., Demmel, J., Dongarra, J., Du Croz, J., Greenbaum, A., Hammarling, S., McKennet, A., Ostrouchov, S., Sorensem, D., 1999, Society for Industrial and Applied Mathematics, Philadephia,PA, third edition

ANSYS, 1994, ANSYS 5.7, Software

ATMEL, ATMega128-Datasheet, rev. 2467oavr10/06 edition

Bayley, A. M., Davis, R. J., Haggis, J. S., Karcher, H., 1994, Astronomy and Astrophysics, 283, 1051

Chiplus, Chiplus, CS18LV10245-Datasheet, 2004

Chiueh, T., Ma, C.-J., 2002, ApJ, 578, 12

Condon, J., 2003a, Technical report, Green Bank Telescope, PTCS/PN/10

Condon, J., 2003b, Technical report, Green Bank Telescope, PTCS/SN/3

Condon, J., Broderick, J., Seielstad, G., 1989, AJ, 97, 1064

Condon, J., Broderick, J., Seielstad, G., 1993, AJ, 106, 1095

Condon, J., Constantikes, K., 2003, Technical report, Green Bank Telescope, PTCS/SN/8,

Condon, J. J., 1997, Publications of the ASP, 109, 166

Deegan, P., AVR Project Makefile Template, http://electrons.psychogenic.com

Doan, C., Liong, S., Department of Civil Engineering, National University of Singapore, Singapore

Dunkels, A., The uIP Embedded TCP/IP Stack, http://www.sics.se/~adam

Emerson, D., 1990, Technical report, NRAO

Gawronski, W., 2002, Technical report, Jet Propulsion Laboratory, CALTECH

Gawronski, W., 2004

Gawronski, W., Souccar, K., 2003

Gaylard, M., 2005a, Hartebeeshoek Radio Astronomy

Gaylard, M., 2005b, Uncertainty Estimates in Fitting a Gaussian Profile

Harp, G., The ATA Servo Loop, 2006

HARTRAO, HARTRAO Radio Telescope Website, `http://www.hartrao.ac.za/`

HARTRAO, HARTRAO Schedule file, `http://www.hartrao.ac.za/nccsdoc/inputfiles/inputs-3.html`

Himwich, W., 1993, Technical report, NASA/Goddard Space Flight Center Space Geodesy Project

Holdaway, M., 1990, Technical report, NRAO

Holdaway, M., 1991, Technical report, NRAO

Holdaway, M., 1997, Technical report, NRAO, 949 N.Cherry Ave, Tucson, AZ, 85721-0655, Memo178

Holmeide, O., Skeie, T., 2001, IEEE, Emerging Technologies and Factory Automation. Proc.

Hunter, T. R., Wilson, R. W., Kimberk, R., Leiker, P. S., 2001, in *Bulletin of the American Astronomical Society*, Vol. 33 of *Bulletin of the American Astronomical Society*, p. 791

Joliffe, I., 2002, Springer

Kaper, H. G., Smits, D. W., Schwarz, U., Takakubo, K., van Woerden, H., 1966, Bulletin Astronomical Institute of the Netherlands, 18, 465

Keating, B., Timbie, P., Polnarev, A., Steinberger, J., 1998, ApJ, 495, 580

King, O., 2006, *Master's thesis*, Rhodes University

Kloth, R., SNTP date and time (UTC) from an NTP time server, `http://www.kloth.net/software/sntp.php`

Kurtz, M., 1991, McGraw-Hill

Kwon, Y., Bang, H., 2000, CRC Mechanical Engineering Series, CRC

Lamb, J., Forster, J., 1993, Technical report, Owens Valley Radio Observatory, California Institute of Technology, MMA Memo 100

Lamb, J., Woody, D., 1998, Technical report, Owens Valley Radio Observatory, California Institute of Technology, MMA Memo 234

Lamb, J., Woody, D., 2002, Proc. URSI General Assembly

MATLAB R14, Chapt. Neural Networks Toolbox, Mathworks

Mills, D., University of Delaware, RFC 2030 - Simple Network Time Protocol (SNTP) Version 4 for IPv4, IPv6 and OSI, 1996

Nise, N., 2000, John Wiley & Sons

Nothnagel, A., Wirtz, C., Sauerbier, M., Sobanski, M., 1997, Proc. 13th Working Meeting on European VLBI for Geodesy and Astrometry

Ogata, K., 1970, Electrical Engineering Series, Prentice-Hall

Ott, H., 2001, Printed Circuit Design Magazine, p. 8

POSITAL FRABA, Absolute Rotary Encoder(SSI)-Datasheet, info@posital.de

Press, W., Teukolsky, S., Vetterling, W., Flannery, B., 2001, Cambridge University Press

Reich, W., 2006, ArXiv Astrophysics e-prints

Rhodes University, 2006, Radio Telescopes and Instrumentation

Rodriguez, E., TCP vs. UDP, `http://www.skullbox.net/tcpudp.php`

Schlens, J., 2005, A Tutorial on Principal Component Analysis

Schwab, C., 2004, The Industrial Ethernet Book

Sinha, N., 1986, Holt,Rinehart and Winston

Sullivan, A., 2001, *Master's thesis*, Rhodes University

Tanenbaum, A., 1996, Prentice-Hall International, Inc

The Mathworks, 2005, MATLAB 7.0, Software

Ukita, N., 1999, Publ. Natl. Astron. Obs. Japan, 5, 139

Ukita, N., Ezawa, H., Mimura, H., Sugamuma, A., Kitazawa, K., Masuda, T., Kawaguch, N., Sugiyama, R., Miyawaki, K., 2001, Publ. of the Natl Astron. Obs. Japan

Von Hoemer, S., 1975, A+A

Wallace, P., 2004, SLALIB Positional Astronomy Software, `http://www.starlink.ac.uk/`

WCS, Introduction to celestial coordinate systems, `http://www.atnf.csiro.au/people/mcalabre/WCS/Intro/WCS11.html`

Westcott, T., 2000, PID without a PHD, `http://www.embedded.com/2000/0010/0010feat3.htm`

Wikipedia, 2007a, Ethernet — Wikipedia, The Free Encyclopedia, [Online; accessed 27-June-2007]

Wikipedia, 2007b, TCP/IP model — Wikipedia, The Free Encyclopedia, [Online; accessed 27-June-2007]

Williams, A., 1981, McGraw-hill book Company

Yaskawa, SERVOPACK-DC Servomotor Controller for Speed Control Type CPCR-MR01C to -MR99C-Datasheet, Document:TSE-C717-12G

Zaldarriaga, M., 2004, in W. L. Freedman (ed.), *Measuring and Modeling the Universe*, p. 309

Part I

Appendix

Appendix A

Elliptical Gaussian Uncertainties

The derivation below is taken from Condon (1997) with less specific reference to Kaper et al. (1966).

The equation for an elliptical Gaussian can be represented as

$$G(x,y) = A\ exp\left[-\frac{(x-x_0)^2}{2\sigma_x^2} - \frac{\beta(x-x_0)(y-y_0)}{\sigma_x\sigma_y} - \frac{(y-y_0)^2)}{2\sigma_y^2}\right] \tag{A.1}$$

A gives the peak amplitude, (x_0, y_0) the central position of the Gaussian, σ_x and σ_y are the RMS lengths of the major and minor axes and β is a measure of the position-angle difference between the principal axes of the ellipse and the coordinate axes (Condon, 1997).

A description of estimating uncertainties for fitting the elliptical Gaussian to images is described by Condon (1997). This method can be used to estimate uncertainties for fitting to this data.

Suppose an image is constructed of m independent amplitude measurements $a_k (k = 1, ...m)$ each having the same Gaussian error distribution with the same RMS μ. If this is the case then the best-fit is one which minimises the sum of the residual variances

$$\chi^2 = \sum_{k=1}^{m} \frac{[a_k - G(x_k, y_k)]^2}{\mu^2} \tag{A.2}$$

The function $G(x, y)$ has 6 (potentially) free parameters (p_i) where $p_1 = A$, $p_2 = x_0$, $p_3 = y_0$, $p_4 = \sigma_x$, $p_5 = \sigma_y$, $p_6 = \beta$. Each of these has one normal equation constraining the fitting

$$\frac{\partial\chi^2}{\partial p_i} = \frac{2}{\mu^2}\sum_{k=1}^{m}[a_k - G(x_k, y_k)]\frac{\partial G(x_k, y_k)}{\partial p_i} = 0 \tag{A.3}$$

Furthermore, if we assume that the residuals are small then we can linearise the normal equations using a Taylor-series approximation

$$[a_k - G(x_k, y_k)] \approx \sum_{j=1}^{n}\frac{\partial G(x_k, y_k)}{\partial p_j}dp_j \tag{A.4}$$

Using Equation A.4, Equation A.3 becomes

$$\frac{2}{\mu^2}\sum_{k=1}^{m}\sum_{j=1}^{n}\frac{\partial G(x_k, y_k)}{\partial p_j}\frac{\partial G(x_k, y_k)}{\partial p_i}dp_j = 0;\ i = 1, ..., n \tag{A.5}$$

To simplify the above we define the above is the $n \times n$ symmetric matrix $\mathbf{D}$ with elements

$$\mathbf{D_{ij}} = \sum_{k=1}^{m}\frac{\partial G(x_k, y_k)}{\partial p_j}\frac{\partial G(x_k, y_k)}{\partial p_i} \tag{A.6}$$

This represents the coefficients of the linearised normal equations. If the data samples cover the main peak of the Gaussian and are uniformly separated by separation h in each coordinate, the sum over k can be approximated by integration.

$$\sum_{k=1}^{m} \frac{\partial G(x_k, y_k)}{\partial p_i} \frac{\partial G(x_k, y_k)}{\partial p_j} \approx \frac{1}{h^2} \int_{-\infty}^{\infty} \int_{-\infty}^{\infty} \frac{\partial G(x, y)}{\partial p_i} \frac{\partial G(x, y)}{\partial p_j} dxdy \tag{A.7}$$

Evaluating these double integrals is most easily accomplished in the limit as $\beta \to 0$ which requires that arbitrary coordinate axes be chosen so that they are nearly parallel to the principal axes of the ellipse (since β is a measure of the angle between the principal axes and the coordinate axes). If we let $p_1 = A$, $p_2 = x_0$, $p_3 = y_0$, $p_4 = \sigma_x$, $p_5 = \sigma_y$, $p_6 = \beta$ then evaluating the double integral results in the coefficient matrix $\mathbf{D}$ given below

$$\mathbf{D} \approx \frac{\pi A}{2h^2} \begin{pmatrix} \frac{2\sigma_x\sigma_y}{A} & 0 & 0 & \sigma_y & \sigma_x & 0 \\ 0 & \frac{A\sigma_y}{\sigma_x} & 0 & 0 & 0 & 0 \\ 0 & 0 & \frac{A\sigma_x}{\sigma_y} & 0 & 0 & 0 \\ \sigma_y & 0 & 0 & \frac{3A\sigma_y}{2\sigma_x} & \frac{A}{2} & 0 \\ \sigma_x & 0 & 0 & \frac{A}{2} & \frac{3A\sigma_x}{2\sigma_y} & 0 \\ 0 & 0 & 0 & 0 & 0 & \frac{A\sigma_x\sigma_y}{2} \end{pmatrix}.$$

A.1 Error Matrix and Error Propagation

The inverse matrix $\mathbf{D^{-1}}$ is called the error matrix because the variance $\mu^2(F)$ of a differentiable function $F(p_1..., p_n)$ of the fitted parameters is

$$\mu^2(F) = \mu^2 \sum_{i=1}^{n} \sum_{j=1}^{n} D_{ij}^{-1} \frac{\partial F}{\partial p_i} \frac{\partial F}{\partial p_j} \tag{A.8}$$

This error matrix for the full 6 parameters is given by

$$D^{-1} \approx \frac{2h^2}{\pi A} \begin{pmatrix} \frac{A}{2\sigma_x\sigma_y} & 0 & 0 & \frac{-1}{2\sigma_y} & \frac{-1}{2\sigma_x} & 0 \\ 0 & \frac{\sigma_x}{A\sigma_y} & 0 & 0 & 0 & 0 \\ 0 & 0 & \frac{\sigma_y}{A\sigma_x} & 0 & 0 & 0 \\ \frac{-1}{2\sigma_y} & 0 & 0 & \frac{\sigma_x}{A\sigma_y} & 0 & 0 \\ \frac{-1}{2\sigma_x} & 0 & 0 & 0 & \frac{\sigma_y}{A\sigma_x} & 0 \\ 0 & 0 & 0 & 0 & 0 & \frac{2}{A\sigma_x\sigma_y} \end{pmatrix}.$$

The diagonal elements of D^{-1} represent the variance such that

$$\mu^2(A) = \mu^2 D_{11}^{-1} \approx \frac{2A^2}{\pi\sigma_x\sigma_y} \left(\frac{h^2\mu^2}{A^2} \right) \tag{A.9a}$$

$$\mu^2(x_0) = \mu^2 D_{22}^{-1} \approx \frac{2\sigma_x}{\pi\sigma_y} \left(\frac{h^2\mu^2}{A^2} \right) \tag{A.9b}$$

$$\mu^2(y_0) = \mu^2 D_{33}^{-1} \approx \frac{2\sigma_y}{\pi\sigma_x} \left(\frac{h^2\mu^2}{A^2} \right) \tag{A.9c}$$

$$\mu^2(\sigma_x) = \mu^2 D_{44}^{-1} \approx \frac{2\sigma_x}{\pi\sigma_y} \left(\frac{h^2\mu^2}{A^2} \right) \tag{A.9d}$$

$$\mu^2(\sigma_y) = \mu^2 D_{55}^{-1} \approx \frac{2\sigma_y}{\pi\sigma_x} \left(\frac{h^2\mu^2}{A^2} \right) \tag{A.9e}$$

$$\mu^2(\beta) = \mu^2 D_{66}^{-1} \approx \frac{4h^2}{\pi\sigma_x\sigma_y} \left(\frac{h^2\mu^2}{A^2} \right) \tag{A.9f}$$

The equations can be simplified if we introduce a parameter describing the signal to noise ratio of the fit. Each independent data point used in constraining the Gaussian fit can be given a statistical weight **proportional to the square of its signal-to-noise ratio**, $\boldsymbol{p_k = G(x_k, y_k)/\mu}$. Quadratically summing over all the data points in the fit produces the number ρ, which is a measure of the overall signal-to-noise ratio of the Gaussian fit.

$$\begin{aligned}\rho^2 &= \sum_{k=1}^{m} \frac{G(x_k, y_k)^2}{\mu} \\ &\approx \frac{1}{h^2\mu^2} \int_{-\infty}^{\infty}\int_{-\infty}^{\infty} G^2(x,y)dxdy \\ &= \frac{\pi\sigma_x\sigma_y}{h^2}\left(\frac{A}{\mu}\right)^2 \end{aligned} \tag{A.10}$$

We see the ρ^2 is the product of two numbers. The first is an effective number $N = \pi\sigma_x\sigma_y/h^2$ of independent samples in the fitted Gaussian and the second is the square of the signal-to-noise ratio of the central sample $\left(\frac{A}{\mu}\right)^2$. Substituting this into equations A.9 leads to

$$\frac{2}{\rho^2} \approx \frac{\mu^2(A)}{A^2} \tag{A.11a}$$

$$= \frac{\mu^2(x_0)}{\sigma_x^2} \tag{A.11b}$$

$$= \frac{\mu^2(y_0)}{\sigma_y^2} \tag{A.11c}$$

$$= \frac{\mu^2(\sigma_x)}{\sigma_x^2} \tag{A.11d}$$

$$= \frac{\mu^2(\sigma_y)}{\sigma_y^2} \tag{A.11e}$$

$$= \frac{\mu^2(\beta)}{2} \tag{A.11f}$$

For astronomers these quantities are usually expressed in terms of the full-width between half-maximum points (FWHM) where the major diameter is $\Theta_M\sqrt{8ln2}\sigma_x$ and the minor diameter is $\Theta_m\sqrt{8ln2}\sigma_y$. The major position angle ϕ is used instead of β which is defined as

$$\frac{(x-x_0)^2}{2\sigma_x^2} + \frac{\beta(x-x_0)(y-y_0)}{\sigma_x\sigma_y} + \frac{(y-y_0)^2}{2\sigma_y^2} = 1 \tag{A.12}$$

For small values of β

$$\lim_{\beta\to 0}\phi = \beta\left(\frac{\sigma_x\sigma_y}{\sigma_y^2 - \sigma_x^2}\right)$$

Using Equation A.8 we can get the error in ϕ as

$$\begin{aligned}\mu^2(\phi) &= \mu^2\left[D_{44}^{-1}\left(\frac{\partial\phi}{\partial\sigma_x}\right)^2 + D_{55}^{-1}\left(\frac{\partial\phi}{\partial\sigma_y}\right)^2 + D_{66}^{-1}\left(\frac{\partial\phi}{\partial\sigma_\beta}\right)^2\right] \\ &\approx \frac{4\sigma_x\sigma_y}{\pi(\sigma_x 2 - \sigma_y^2)^2}\left(\frac{h^2\mu^2}{A^2}\right) \end{aligned} \tag{A.13}$$

Equation A.13 is only valid for $\mu^2(\phi) \ll 1$

Using these quantities we arrive at

$$\rho^2 = \frac{\pi}{8ln2}\frac{\Theta_M\Theta_m A^2}{h^2\mu^2} \tag{A.14}$$

The uncertainties are given by

$$\frac{2}{\rho^2} \approx \frac{\mu^2(A)}{A^2} \tag{A.15a}$$

$$= 8ln2\frac{\mu^2(x_0)}{\Theta_M^2} \tag{A.15b}$$

$$= 8ln2\frac{\mu^2(y_0)}{\Theta_m^2} \tag{A.15c}$$

$$= \frac{\mu^2(\Theta_M)}{\Theta_m^2} \tag{A.15d}$$

$$= \frac{\mu^2(\Theta_m)}{\Theta_m^2} \tag{A.15e}$$

$$= \frac{\mu^2(\phi)}{2}\left(\frac{\Theta_M^2 - \Theta_m^2}{\Theta_M\Theta_m}\right)^2 \tag{A.15f}$$

In using these equations for my estimates of uncertainty, I calculated the noise (μ) by using the RMS value of the first 40 data points, which I assumed were sampled when the beam was not on source. I used a sample spacing interval (h) which I obtained from the scans.

A.2 Estimates of Uncertainties in this data

Pointing offsets were obtained from observations by fitting elliptical Gaussians to point source observations. The relationships described above were used to estimate the uncertainties of the pointing offsets derived using this method. These are shown in Figure A.1. From the figure it is clear that the magnitude of the error is significantly less than the target pointing offset of 4 mdeg and, for this reason, I have treated these uncertainties as negligible.

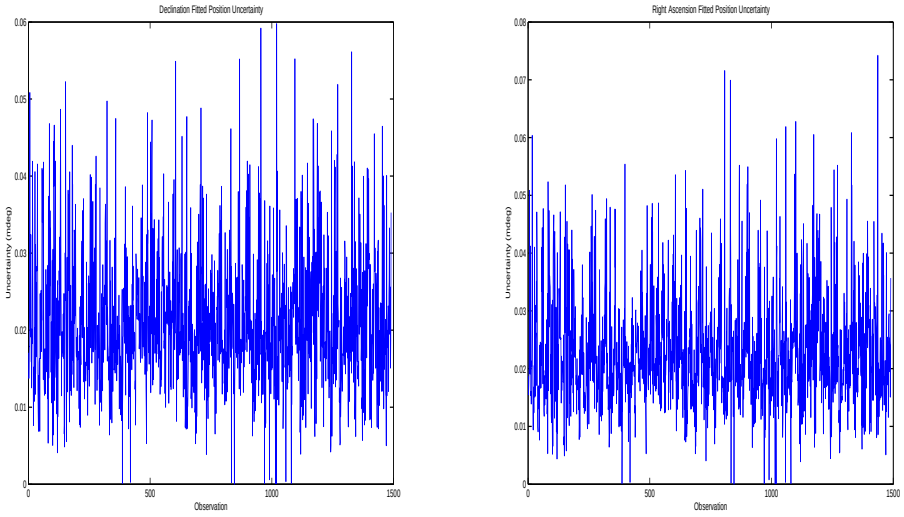

(a) Estimated errors in the Declination Position estimated from the 3-D Gaussian fitting

(b) Estimated errors in the Right Ascension Position estimated from the 3-D Gaussian fitting

Figure A.1: Typical uncertainties in position estimated using a 3-D Gaussian. The values are all much less than 1 mdeg and thus are not significant in the context of this project.

Appendix B

VLBI Parameter listing

B.1 Description of the model and parameters

The VLBI pointing model is parameter based and has the form shown below. It is described in detail by Himwich (1993).

$$\begin{aligned}\Delta X &= P_1 - P_2\cos\phi\sin X\sec Y + P_3\tan Y - P_4\sec Y + P_5\sin X\tan Y \\ &\quad -P_6\cos X\tan Y + P_{12}X + P_{13}\cos X + P_{14}\sin X + P_{15}\cos 2X \\ &\quad +P_{16}\sin 2X \qquad \text{(B.1)}\\ \Delta Y &= P_5\cos X + P_6\sin X + P_7 - P_8(\cos\phi\cos X\sin Y - \sin\phi\cos Y) \\ &\quad +P_9Y + P_{10}\cos Y + P_{11}\sin Y \qquad \text{(B.2)}\end{aligned}$$

For the HartRAO Antenna X is the Hour Angle, Y is the Declination and ϕ is the geodesic latitude (25.8873° S) at HARTRAO, however the model is suitable for use with other local coordinate systems.

P_1 is the X-angle offset, the difference of the X-angle encoder bias (positive if encoder reading is too high) minus 'tilt around', which is the tilt of the antenna around the Y =90°. (positive if apparent X,Y=(0°,0°) is closer to true X,Y=(+90°,0°)).

P_2 is the X angle sag, the effect of gravity on the RF axis of the dish projected on the X direction (positive if the RF axis is lower)

P_3 is the perpendicular axis skew, the apparent Y =+90° to true Y =0° plane lack of orthogonality in the plane perpendicular to the current X angle meridian (positive if apparent Y=+90° is closer to true X,Y=((current X)-90))

P_4 is the box offset, RF-axis to radial direction misalignment along the X direction (positive if RF-axis is toward the increasing X angle direction)

P_5 is the "tilt out", tilt of the apparent Y=+90 toward the true X,Y=(0,0) position (positive if apparent Y=+90 is closer to true X,Y=(0,0))

P_6 is the "tilt over", tilt of the Y=+90 toward the X,Y=(+90 ,0) position (positive if apparent Y=+90 is closer to true X,Y=(+90,0)

P_7 is the Y angle offset, difference of the Y angle encoder bias (positive if encoder reads too high) minus the sum of the skew of Y=+90 along the current X meridian angle (positive if apparent Y=+90 is farther from true X,Y=(current X, 0)) plus the RF axis to radial direction misalignment along the Y direction (positive if the RF axis is toward the increasing Y angle direction)

P_8 is the Y angle sag, the effect of gravity on the RF axis of the dish projected on the Y direction (positive if the RF axis is lower)

P_9 is an *ad hoc* Y-angle excess scale factor (greater than 0 if the encoder read-out changes faster than the actual antenna position)

P_{10} is an *ad hoc* $Y \cos Y$ coefficient

P_{11} is an *ad hoc* $Y \sin Y$ coefficient

P_{12} is an *ad hoc* X-angle excess scale factor (greater than 0 if the encoder read-out changes faster than the actual antenna position)

P_{13} is an *ad hoc* $X \cos X$ coefficient

P_{14} is an *ad hoc* $X \sin X$ coefficient

P_{15} is an *ad hoc* $X \cos 2X$ coefficient

P_{16} is an *ad hoc* $X \cos 2X$ coefficient

B.2 Discussion of Model

The model is an attempt to explain and quantify two primary effects found in telescopes.

- Misalignments in the coordinate system
- Gravitational deformation and other *ad hoc* terms

The parameters P_1, P_3, P_4, P_5, P_6 and P_7 are representative of misalignments of the RF feed with all the other parameters representing gravitational deformations or *ad hoc* terms.

Table B.1: VLBI Pointing Model Parameters

Description	Original	Refitted	% Change
P_1	-0.0074075498	-0.01049454780367	29.4153
P_2	-0.0063556978	-0.00686492941186	7.4179
P_3	-0.0047638724	-0.00517999928007	8.0333
P_4	-0.0024362272	-0.00279710700103	12.9019
P_5	0.0544945337	0.05452390127463	0.0539
P_6	-0.0207822602	-0.02080699817014	0.1189
P_7	-0.0595969707	-0.05996367310289	0.6115
P_8	-0.0234767608	-0.02450930739531	4.2129
P_9	0	-0.00110319602355	100.0000
P_{10}	0	-0.00023846410765	100.0000
P_{11}	0.0173795968	0.01756346900581	1.0469
P_{12}	0	0.04962180835857	100.0000
P_{13}	0	0.00339941490416	100.0000
P_{14}	-0.0355144888	-0.10342461981940	65.6615
P_{15}	0	-0.00085846903721	100.0000
P_{16}	0	0.00893371292985	100.0000